



# Break through the strength-ductility trade-off dilemma in aluminum matrix composites via precipitation-assisted interface tailoring

Yu Ma, Han Chen, Ming-Xing Zhang, Ahmed Addad, Yi Kong, Matthieu  
Lezaack, Weiming Gan, Zhe Chen, Gang Ji

## ► To cite this version:

Yu Ma, Han Chen, Ming-Xing Zhang, Ahmed Addad, Yi Kong, et al.. Break through the strength-ductility trade-off dilemma in aluminum matrix composites via precipitation-assisted interface tailoring. *Acta Materialia*, 2023, 242, pp.118470. 10.1016/j.actamat.2022.118470 . hal-04255448

**HAL Id: hal-04255448**

**<https://hal.science/hal-04255448>**

Submitted on 24 Oct 2023

**HAL** is a multi-disciplinary open access archive for the deposit and dissemination of scientific research documents, whether they are published or not. The documents may come from teaching and research institutions in France or abroad, or from public or private research centers.

L'archive ouverte pluridisciplinaire **HAL**, est destinée au dépôt et à la diffusion de documents scientifiques de niveau recherche, publiés ou non, émanant des établissements d'enseignement et de recherche français ou étrangers, des laboratoires publics ou privés.

# Break through the strength-ductility trade-off dilemma in aluminum matrix composites via precipitation-assisted interface tailoring

Yu Ma<sup>a,b,c,1</sup>, Han Chen<sup>c,1</sup>, Ming-Xing Zhang<sup>d</sup>, Ahmed Addad<sup>a</sup>, Yi Kong<sup>e</sup>, Matthieu B. Lezaack<sup>f</sup>, WeiMing Gan<sup>g</sup>, Zhe Chen<sup>c,\*</sup>, Gang Ji<sup>a,\*</sup>

a. Univ. Lille, CNRS, INRAE, Centrale Lille, UMR 8207 - UMET - Unité Matériaux et Transformations, F-59000 Lille, France

b. Institute of Engineering Thermophysics, Chinese Academy of Sciences, Beijing 100190, PR China

c. State Key Laboratory of Metal Matrix Composites, Shanghai Jiao Tong University, Shanghai 200240, China

d. School of Mechanical and Mining Engineering, University of Queensland, St Lucia, QLD, 4072, Australia

e. State Key Laboratory of Powder Metallurgy, Central South University, Changsha 410083, China

f. Institute of Mechanics, Materials and Civil Engineering, Université catholique de Louvain, B-1348 Louvain-la-Neuve, Belgium

g. German Engineering Materials Science Centre, Helmholtz-Zentrum Geesthacht, D-21502 Geesthacht, Germany

\*Corresponding authors: Dr. Zhe Chen (zhe.chen@sjtu.edu.cn); Dr. Gang Ji (gang.ji@univ-lille.fr)

Yu Ma<sup>1</sup> and Han Chen<sup>1</sup> are the co-first author of this work

## Abstract

Strength-ductility trade-off is usually an inevitable scenario in most engineering materials, including metal matrix composites (MMCs) where reinforcement particles significantly degrade ductility. The decrease of ductility is mainly attributed to dislocation pile-ups at the high mismatch interface between reinforcement particles and matrix, which can't lead to effective dislocation multiplication and annihilation, finally leading to a low work hardening rate. To address this challenge, herein we propose a precipitation-assisted interface tailoring (PAIT) mechanism to improve the coherency of interface between reinforcement particles and matrix by introducing an interphase (IP). To achieve this PAIT mechanism, we design a manufacturing process combining the conventional casting, friction stir processing (FSP), hot extrusion with heat treatment. A TiB<sub>2</sub>/Al-Zn-Mg-Cu composite fabricated with this process shows higher strength and ductility, which stand out from most available Al-based materials. In this composite, a Mg(Zn<sub>1.5</sub>Cu<sub>0.5</sub>) IP is introduced to improve the coherency and strength of the TiB<sub>2</sub>/Al interface by transforming the high mismatch TiB<sub>2</sub>/Al interface into the low mismatch TiB<sub>2</sub>/IP/Al multi-interfaces (i.e. sandwich structure). This effectively promotes dislocation multiplication and subsequent dislocation annihilation to increase the work hardening rate by restricting the dislocation pile-ups surrounding the interface, thus leading to a higher ductility. Our study aims

to overcome the strength-ductility trade-off of MMCs by tailoring interface structure, which can provide insight into the production of high-performance MMCs.

**Keywords:** Metal matrix composites (MMCs); Nanoparticles; Interfacial misfit; Mechanical properties; Dislocation

## 1. Introduction

Strength and ductility are two baseline mechanical properties in metals. However, they are usually mutually exclusive, i.e. a gain in strength is inevitably at the cost of ductility and vice versa [1,2]. Thus, solving this strength-ductility trade-off dilemma has always been a long-term challenge to material researchers and engineers. With the rise of novel nanocrystalline materials [3,4], a number of successful strategies have been reported in the past decades, such as introducing nano-twins [5], gradient nanograined structures [6], lamella [7], hierarchical defects [8], and chemical boundaries [9] into metals. Generally, their common ground aimed at promoting a **work hardening rate** to stabilize uniform plastic deformation by intentionally generating heterogeneous nanostructures. Despite the promising results, most of previously reported nanomaterials were produced in laboratories, and the cost are usually soaring due to their complicated processing technologies, which limits their industrial applications.

Metal matrix composites (MMCs) integrate reinforcements into a metal matrix, leading to improved mechanical performance, particularly in the case that high strength and Young's modulus are necessary [10,11]. As one of the typical nanoscale heterogeneities, ceramic nanoparticles (CNPs) and carbon nanotubes (CNTs) have been widely used as the reinforcements and been verified the success in enhancing the **work hardening rate** with delaying in plastic instability [12,13]. It was thus expected, at least theoretically, that MMCs have a strong potential to evade the strength-ductility trade-off. In addition, the CNPs and CNTs are thermally stable as reinforcements in the composites and production scaling up is possible, which makes such materials even more attractive. However, the current production of composites encounters two critical problems that restrict their industrial applications.

The first one is the difficulty to uniformly disperse nanosized reinforcements in a metal matrix, especially via conventional casting [14,15]. At nucleation stage of metal solidification, the introduced CNPs tend to agglomerate in the melt due to their attractive van der Waals forces

[16]. As a result, such nanosized reinforcements are rejected to the solidification front as clusters during growth process and subsequently segregate along grain boundaries in the casting [17]. The nanosized reinforcement clusters along grain boundaries can cause severe stress concentrations during forming process or application, which significantly lowers the ductility of MMCs [18]. Another issue is the low interface coherency, which weakens bonding strength between the reinforcement and the metal matrix even though the distribution of the reinforcement can be dispersed and homogenized [19,20]. Since the conventional CNP/metal interface is incoherent, the gliding dislocations can be easily trapped and piled up at the interfaces during plastic deformation, giving rise to stress concentration [21-23]. The dislocation pile-ups also inhibit the subsequent dislocation movement and multiplication, leading to strain localization and plastic instability, which lowers ductility.

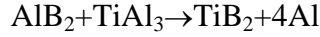
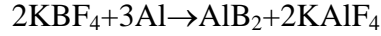
To solve as above-mentioned problem of strength-ductility trade-off, dispersing the CNPs and enhancing their interfacial coherency with the matrix become essential and critical. Here we report a new design strategy, consisting of a three-step microstructure optimization process, to fabricate Al-based composites with superior balance of strength and ductility. The first step is to *in-situ* introduce CNPs into the Al matrix, acquiring ‘clean’ semi-coherent CNP/Al interfaces, which facilitate the subsequent interface precipitation [24]. Second, we conducted severe plastic deformation to evenly disperse the high-density CNPs within Al grains. This is finally followed by heat treatment transforming the initial high mismatch CNP/Al interface into the CNP/interphase (IP)/Al multi-interfaces via precipitation-assisted interface tailoring (PAIT) mechanism to further enhance the CNP/Al coherency. To validate this design strategy, we selected and fabricated a  $\text{TiB}_2$  nanoparticles reinforced Al-Zn-Mg-Cu (7075Al) matrix composite (hereafter called  $\text{TiB}_2/7075\text{Al}$ ) as an example material because  $\text{TiB}_2$  is a common grain refiner for cast Al alloys and ingots [25].

## **2. Materials and Methods**

### ***2.1 Sample preparation***

The  $\text{TiB}_2/7075\text{Al}$  composite sample was fabricated using the mixed-salt reaction cast method initially developed by the London scandinavian metallurgical company [24]. First,  $\text{K}_2\text{TiF}_6$  and  $\text{KBF}_4$  reactive salts with high purity were mixed and added into molten Al metal in a high-purity graphite crucible heated at 900 °C in an electrical resistance furnace. The melt was

mechanically stirred at 600 rpm for 15 min, and then poured into a permanent mould to acquire the pure Al composite reinforced with pre-synthesized master TiB<sub>2</sub>. Exothermal reactions associated with this in-situ casting process are following:



Then, the pre-synthesized master TiB<sub>2</sub>/Al composite was re-melted by electrical resistance furnace and Mg, Zn and Al-Cu master alloy were added into the melt followed by direct chill casting. Chemical composition of the as-produced sample measured by inductively coupled plasma atomic emission spectroscopy analysis was 6.9 wt.% Zn, 2.3 wt.% Mg, 2.4 wt.% Cu and 4.5 wt.% TiB<sub>2</sub>. The volume fraction of TiB<sub>2</sub> particles is 2.2 vol.%, which is obtained from mass fraction conversion. The TiB<sub>2</sub>/7075Al composite plates with a large dimension were cut from the cast ingot and annealed at 470 °C for 24 h. As detailed in our previous work [26], an optimized (4-pass) FSP process with a tool rotation rate of 600 rpm, a tool tilt angle of 2.5°, a traverse speed of 80 mm/min and a processing depth of 8 mm was carried out on the plates. The samples cut from the nugget zone were homogenized at 470 °C for 24 h and then extruded at 420 °C using the extrusion ratio of 20:1. Followed by this, the as-extruded samples were subjected to solution treatment at 477 °C for 70 min, water quenching (WQ) to the room temperature (referred as TiB<sub>2</sub>/7075Al-WQ), and finally peak aging (PA) at 120 °C for 24 h (referred as TiB<sub>2</sub>/7075Al-PA). Both WQ and PA composite samples together with a PA 7075 alloy sample (for comparison, referred as 7075Al-PA) were used for tensile testing and microstructure characterization. As detailed in [27], the alloy sample was subjected to the FSP and PA processes being comparable to those used for the composite samples.

## ***2.2 Microstructure Characterization using electron microscopy***

The samples for scanning electron microscopy (SEM) were cut from the center of the as-extruded plates and were subjected to mechanical grinding and fine polishing. Grain structure and fracture surface were examined using a Joel JSM-7800F microscope equipped with an energy dispersive spectrometer (EDS) and an electron back-scattered diffraction (EBSD) detectors both from Oxford instruments. Post-treatment of the data analyzed by orientation imaging microscopy (OIM) was done using CHANNEL 5.0 software package in order to obtain

information on grain size distribution. The OIM maps were recorded with the step size of 200 nm.

For transmission electron microscopy (TEM) characterization, the standard disk samples with 3 mm in diameter were punched from a thin foil with the thickness of around 70-80  $\mu\text{m}$  obtained by mechanical polishing. A GATAN model 691 precision ion polishing system was used for final ion milling. A state-of-the-art ThermoFisher Titan Themis 60-300 microscope equipped with a probe aberration corrector, operated at 200 kV, was used to acquire (high-resolution) scanning TEM ((HR)STEM) images. Probe size was set to 0.1 nm with a convergence semi-angle of 22.5 mrad. Collection angles of the annular dark-field (ADF) and high-angle ADF (HAADF) detector were set in the range of 10-40 and 80-150 mrad, respectively. The bright and dark contrasts of the Al-Zn-Mg-Cu matrix in a Z-contrast HAADF image can be considered as Zn (Cu)-rich and Mg-rich areas, respectively. The equipped highly efficient (4 quadrant) EDS system was used for chemical analyses of possible precipitates formed at the  $\text{TiB}_2/\text{Al}$  interface. Interface characterization was carried out by tilting the Al matrix to the [110] orientation in terms of the well-documented preferential orientation relationships of the  $\text{TiB}_2/\text{Al}$  interface [28].

### ***2.3 Synchrotron radiation X-ray diffraction (SRXRD) and tensile tests***

The SRXRD was conducted at the high energy materials science (HEMS) beamline P07B operated by the Helmholtz-Zentrum Hereon at PETRA III, DESY. During the SRXRD tests, the wavelength of X-ray was 0.14235 Å, and its incident beam size was  $0.7 \times 0.7 \text{ mm}^2$ . A Perkin Elmer XRD 1622 flat panel detector with  $2048 \times 2048$  pixels and a pixel size of  $200 \times 200 \mu\text{m}^2$  was used for obtaining diffraction patterns. The specimen-to-detector distance was 1433 mm, which was calibrated using a  $\text{LaB}_6$  powder standard. Dislocation density of the samples was measured from SRXRD using the multiple whole profile (MPW) method for line profile analysis [29-31]. In this method, one obtains the Fourier transforms of peak profiles by fitting the Fourier coefficients of *ab initio* physical functions of the size and strain profiles. The corresponding fitting parameters are median and the variance of the size distribution function, dislocation density, dislocation arrangement and dislocation contrast factors. It should be noted that the measured pattern is separated into single diffraction peaks first, since this method focuses on individual profiles. This separation can be achieved by a special program, namely MKDAT. During fitting, the intensities of diffraction peaks are not interpreted physically, thus the intensity of

measured profiles, Fourier-transforms, and fitting theoretical functions are normalized by dividing their maximum values in the fitting procedure. The theoretical functions of MPW and the detailed fitting procedures can be found in Refs. [29-31].

Tensile tests were conducted along the extrusion direction on a Zwick/Roell Z100 instrument using a strain rate of  $10^{-4} \text{ s}^{-1}$  at the room temperature. The dog-bone specimens with the gauge dimensions of  $2 \times 3 \times 15 \text{ mm}^3$  was used. The values of mechanical properties of the samples given in Table 2 are the average of 3 measurements.

#### ***2.4 Edge-to-edge matching (E2EM) modeling and first-principles calculations***

The E2EM model considers that the maximum atomic matching across an interface between two crystals can be achieved through matching along atomic rows (matching directions) that are normally along the close packed or nearly close packed directions in both crystals. These atomic rows are contained in planes (matching planes) that are also close packed or nearly close packed. The atomic matching is defined by the misfit along the matching directions and the mismatch between the matching planes. The major advantage of the E2EM model over other crystallographic models is its capacity to deal with crystals with complicated structure [32]. The matching directions and matching planes of the crystals can be identified and the corresponding misfits and mismatches can be calculated and possible crystallographic orientation relationships between any two phases can be investigated [33,34].

First-principles calculations were performed with the Vienna Ab initio Simulation Package (VASP) code [35,36] implementing the projector augmented wave method. The exchange and correlation effects are described by generalized gradient corrections proposed by Perdew et al. [37]. The cut-off energy for the plane-wave expansion was set as 500 eV for all the calculations, together with accurate precision using in VASP. The convergence criteria for the total energy and forces were set to  $10^{-5} \text{ eV/atom}$  and  $10^{-2} \text{ eV/\AA}$  for all the structure relaxation, together with Methfessel-Paxton smearing scheme of order 2. For interface models containing more than 100 atoms, only Gamma point was used in k-mesh, as well as only ionic positions are allowed to relax. The real-space projection scheme was used for cells containing more than about 30 atoms.

The work of adhesion ( $W_{\text{ad}}$ ) is usually used to investigate the stability of the interface. Larger value of work of adhesion means stronger cohesion of the interface. As an example, the  $W_{\text{ad}}$  of  $\text{TiB}_2/\text{Al}$  interface is calculated as:

$$W_{ad} = \frac{1}{A} (E_{Al} + E_{TiB_2} - E_{int}) \quad (1)$$

where A is the area of the interface,  $E_{Al}$  is the energy of Al slab,  $E_{TiB_2}$  is the energy of  $TiB_2$  slab, and  $E_{int}$  is the energy of the interface model.

### 3. Results and analysis

#### 3.1 Microstructure characterization

Fig. 1 shows the equiaxed grain structures of the 7075Al-PA and  $TiB_2$ /7075Al-PA samples in three dimensions. The average grain sizes in the ED, LT and ST directions of the 7075-PA sample are very close of around 4.41, 4.00, and 3.94  $\mu m$ , respectively. Comparatively, the  $TiB_2$ /7075Al-PA sample also has a uniformly distributed grain structure; however, the average grain sizes in the ED, LT and ST directions are smaller of around 2.67, 2.51, and 2.98  $\mu m$ , respectively. Note that the grain structure and size of the 7075Al-WQ and  $TiB_2$ /7075Al-WQ samples are almost the same as their corresponding 7075Al-PA and  $TiB_2$ /7075Al-PA samples. They are not shown here for the reason of simplicity.



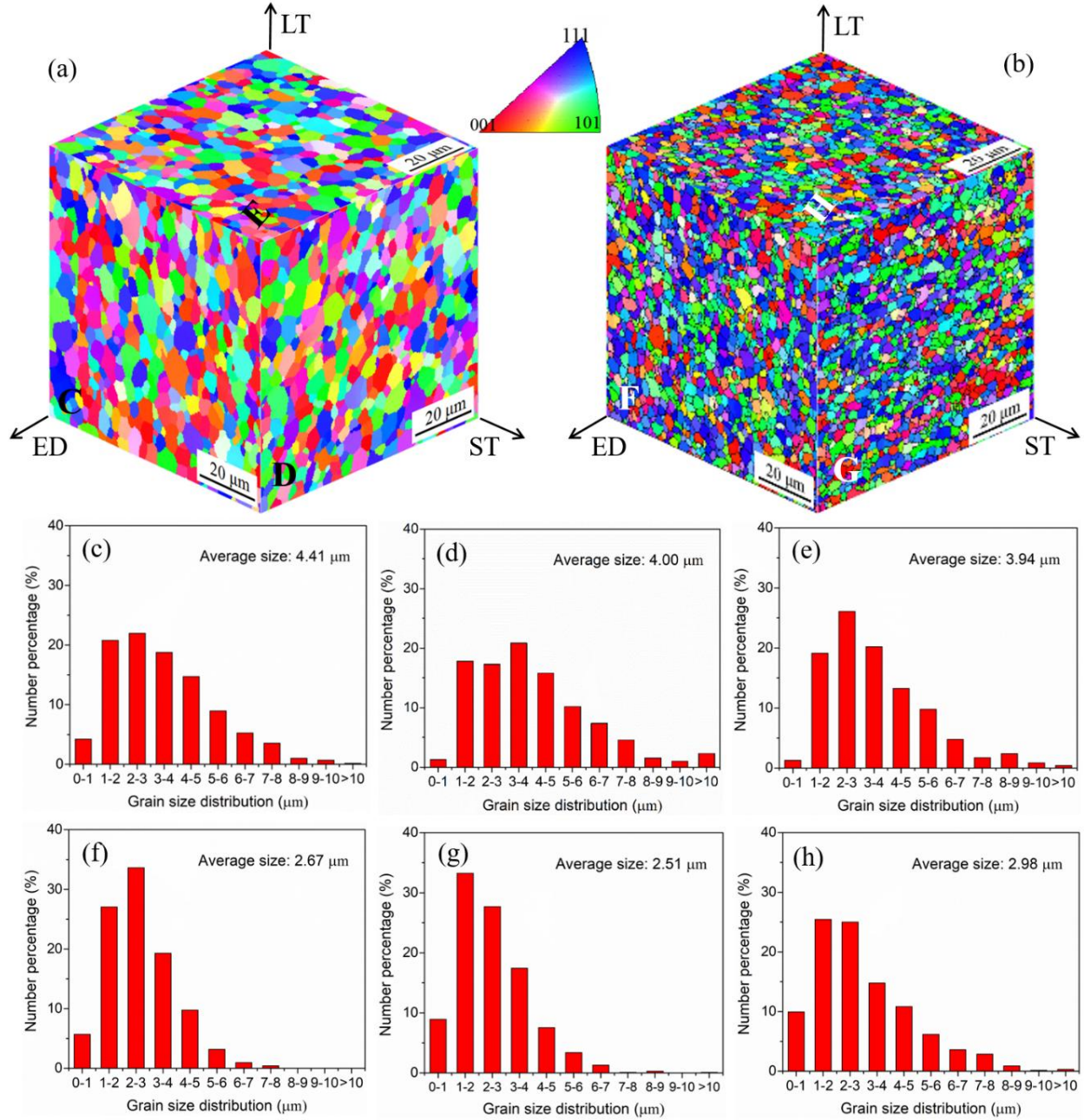


Fig. 1 Grain structures of the 7075Al-PA and TiB<sub>2</sub>/7075Al-PA samples: (a) and (b) reconstructed 3D inverse pole figure maps of the 7075Al-PA and TiB<sub>2</sub>/7075Al-PA samples, respectively; (c-e) corresponding grain size distributions of C, D, and E cross-sections in (a); (f-h) corresponding grain size distributions of F, G, and H cross-sections in (b); ED, LT and ST in (a) and (b) indicate extrusion, long transverse and short transverse directions, respectively.

Fig. 2 shows the distribution and morphology of  $\text{TiB}_2$  particles in the  $\text{TiB}_2/7075\text{Al-WQ}$  and  $\text{TiB}_2/7075\text{Al-PA}$  samples. For the  $\text{TiB}_2/7075\text{Al-WQ}$  sample, the  $\text{TiB}_2$  particles are distributed uniformly in the grain interior (Fig. 2(a-c)). According to our previous study, the size distribution of  $\text{TiB}_2$  particles in such a composite prepared by *in-situ* synthesis follows a log-normal distribution [38]. It was also quantitatively determined by SRXRD that the majority of  $\text{TiB}_2$  particles range from several tens to hundreds of nanometers in diameter, and the average radius size is about 50 nm [38]. The typical  $\text{TiB}_2$  particle has a faceted shape with identified basal, prismatic and pyramidal facets, which corresponds to  $\{0001\}$ ,  $\{01\bar{1}0\}$  and  $\{01\bar{1}1\}$ , respectively (Fig. 3(a)). For the  $\text{TiB}_2/7075\text{Al-PA}$  sample, the homogeneous distribution of  $\text{TiB}_2$  particles in the grain interior remains unchanged, and the interface precipitation phenomena are largely visible (Fig. 2(d-i)). Since the  $\text{TiB}_2/\text{Al}$  interface is tightly bonded and free of oxides due mainly to *in-situ* formation. The PA treatment facilitates the precipitation of IP at the  $\text{TiB}_2/\text{Al}$  interfaces following the specific orientation relationships between  $\text{TiB}_2$  and Al matrix as will be discussed later in section 3.2. Due to the introduction of IP, the  $\text{TiB}_2/\text{IP}/\text{Al}$  multi-interface (i.e. sandwich structure) forms in the  $\text{TiB}_2/7075\text{Al-PA}$  sample (Fig. 3(a)). The EDS maps of Zn, Mg and Cu elements show that this IP is Zn, Mg and Cu rich (Fig. 2(f-i)). The FFT pattern of this IP matches well with the structure of  $\text{Mg}(\text{Zn}_{1.5}\text{Cu}_{0.5})$  phase, as shown in Fig. 3(b) (Hexagonal,  $a = 5.124$ ,  $c = 16.820$  Å,  $P63/mmc$ , No. 194) [39]. Moreover, the measured interplanar spacing of the (0004) and  $(\bar{1}\bar{1}20)$  planes of IP are 0.420 nm and 0.254 nm, respectively, which also agrees with that of the  $\text{Mg}(\text{Zn}_{1.5}\text{Cu}_{0.5})$  phase (Fig. 3(c) and 3(d)). Thus, this IP is determined as the  $\text{Mg}(\text{Zn}_{1.5}\text{Cu}_{0.5})$  phase. Regarding this, more details can be found in our previous study [33].



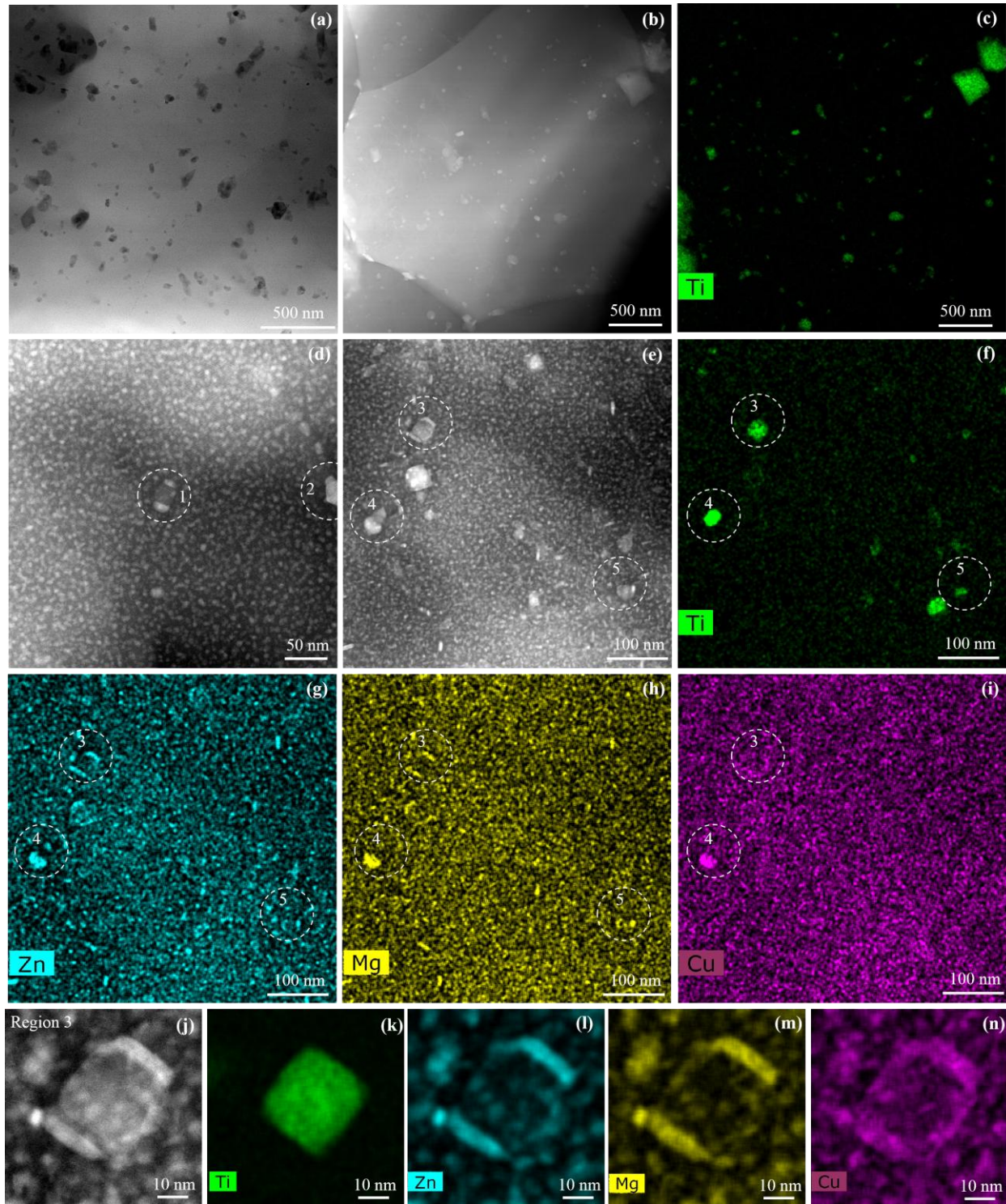


Fig. 2 Distribution and morphology of  $\text{TiB}_2$  particles in (a-c) the  $\text{TiB}_2/7075\text{Al-WQ}$  and (d-i) the  $\text{TiB}_2/7075\text{Al-PA}$  samples: (a-b) TEM bright-field and STEM-HAADF images showing the uniform dispersion of  $\text{TiB}_2$  nanoparticles in the grain interior; (c) the corresponding EDS map of Ti element of (b); (d-e) TEM bright-field images showing the uniform dispersion of  $\text{TiB}_2$  nanoparticles in the grain interior of the  $\text{TiB}_2/7075\text{Al-PA}$  sample; (f-i) the corresponding EDS

maps of Ti, Zn, Mg and Cu elements of (e); (j-n) the magnified STEM-HAADF image and corresponding EDS maps of Ti, Zn, Mg and Cu elements in region 3 of (e). The interfacial precipitation phenomena are observed in the  $\text{TiB}_2$ /7075Al-PA sample, and some of them are represented by dashed white circles numbered 1-5. Note that high magnification is necessary to reveal Cu enrichment in the interface area with tiny interphase of a few nm in size, since the content of Cu is much lower than those of Zn and Mg in  $(\text{Zn}_{1.5}\text{Cu}_{0.5})\text{Mg}$  interphase.

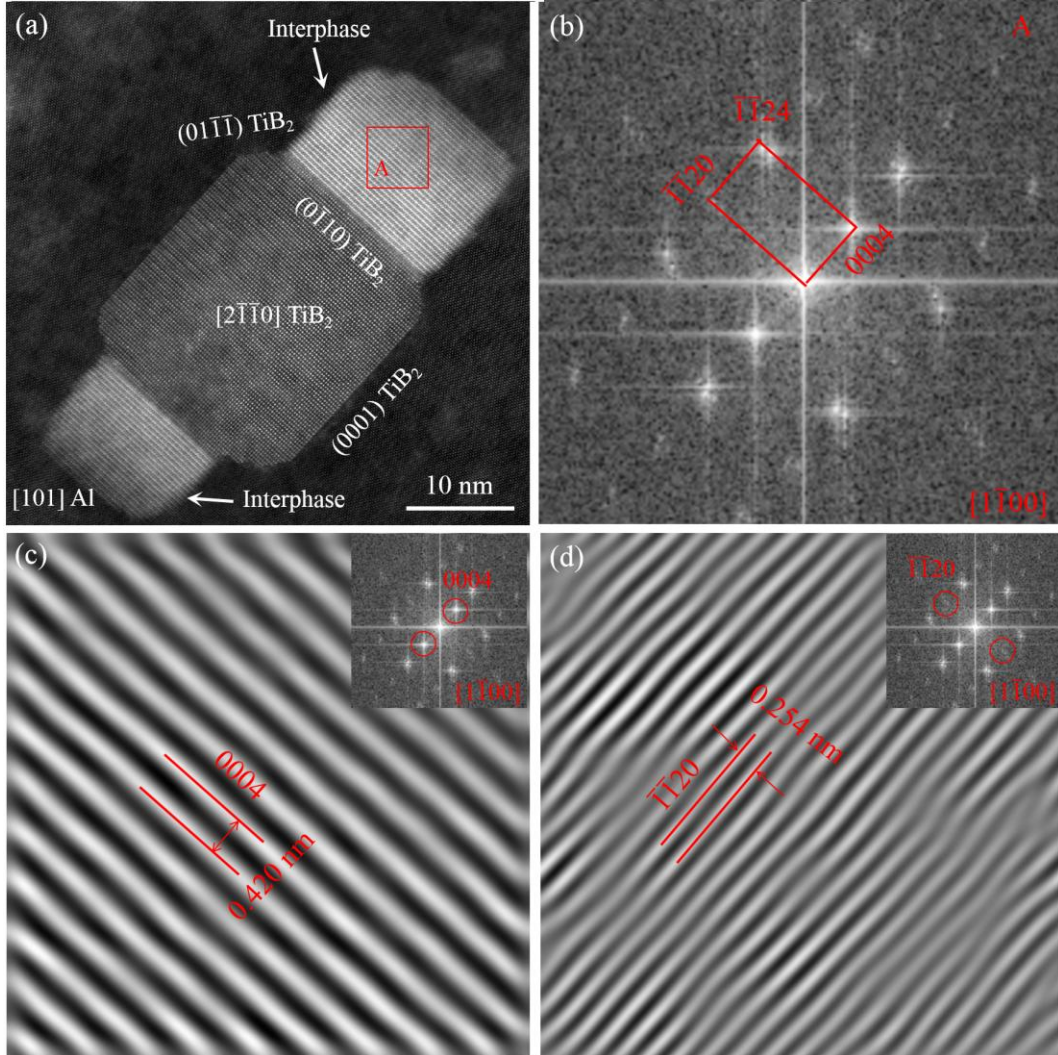


Fig. 3 The interfacial precipitation phenomenon and identification of IP in the  $\text{TiB}_2$ /7075Al-PA sample: (a) STEM-HAADF image showing the  $\text{TiB}_2$ /IP/Al sandwich structure; (b) fast fourier transform (FFT) of IP of the red area A in (a); (c) and (d) inverse FFT (IFFT) images of IP of the red area A in (a) with using different reflection pairs selected in corresponding FFT patterns in insets.



In addition to IP, a high density of homogeneously distributed finer nanoprecipitates are also precipitated within the Al grains away from the  $\text{TiB}_2/\text{Al}$  interfaces (Figs. 2(d), 2(e) and 4(a)). They are fully coherent with the Al matrix, including plate-like GP zones and rectangle  $\eta'$  phase (Fig. 4). The average radius size of these nanoprecipitates is about 3 nm in Fig. 4(a). In the study of Liu *et al.* [40], the average radius size and volume fraction of nanoprecipitates in Al-6.7Zn-2.3Mg-2.4Cu (wt.%) alloy after PA, measured by small angle X-ray diffraction, are around 2.81 nm and 1.41%, respectively. Comparatively, our material has the very similar chemical composition and average radius size of nanoprecipitates. Thus, the volume fraction of 1.41% and the average radius size of 2.81 nm are reasonably proposed to estimate the precipitation strengthening increment in the following discussion.

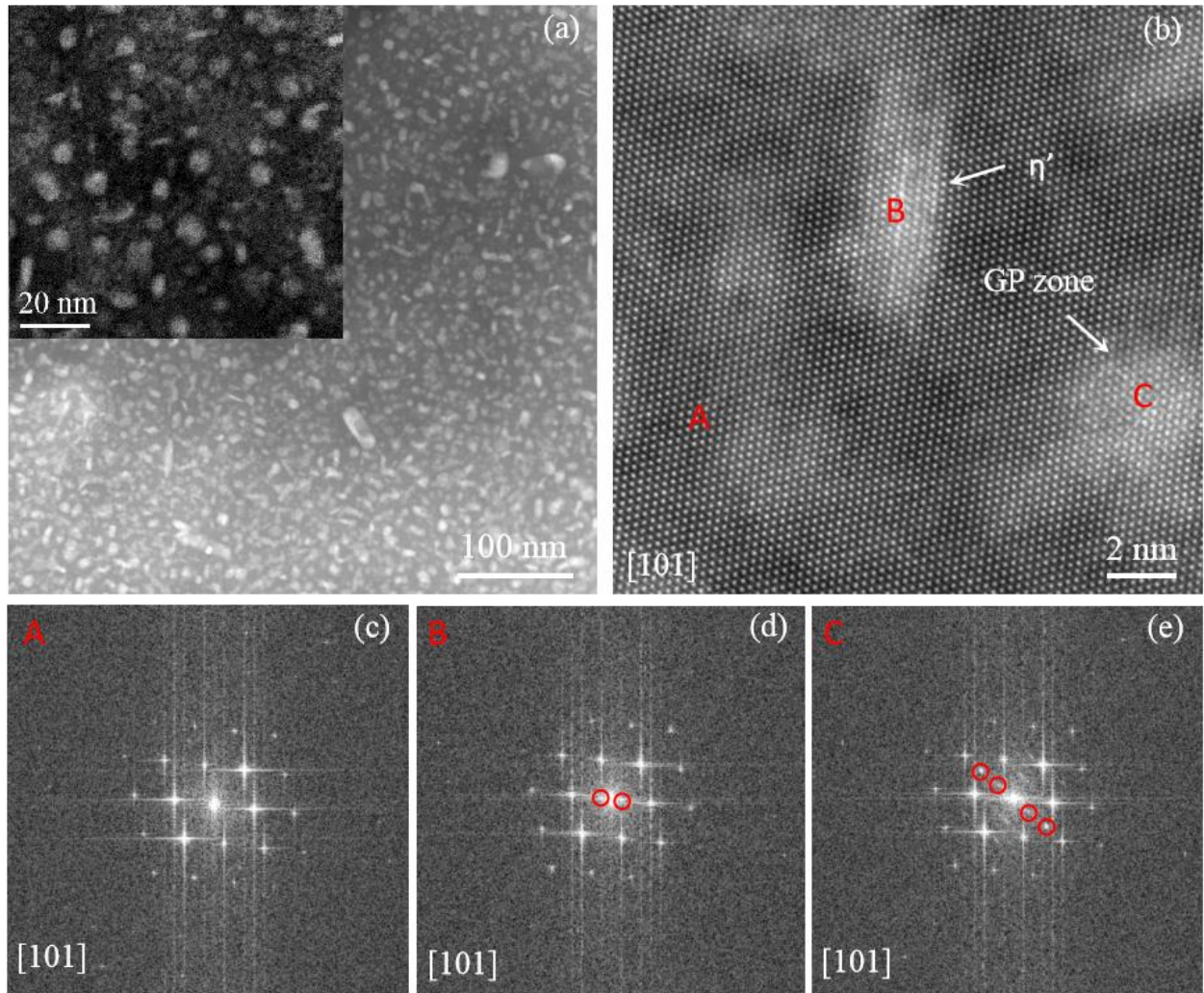


Fig. 4 STEM-HAADF images of precipitates in TiB<sub>2</sub>/7075Al-PA sample: (a-b) plate-like GP zones and rectangle  $\eta'$  phase; (c-e) the corresponding FFT images of A, B, C areas in (b). Here A, B and C represent Al matrix,  $\eta'$  phase and GP zones; respectively.

### 3.2 TiB<sub>2</sub>/Al interface tailoring

Two common crystallographic orientation relationships between TiB<sub>2</sub> particle and Al matrix have been reported in our previous study [33]. One is  $[2\bar{1}\bar{1}0]_{\text{TiB}_2} // [101]_{\text{Al}}$ ,  $(0001)_{\text{TiB}_2} // (\bar{1}11)_{\text{Al}}$ , and the other is  $[2\bar{1}\bar{1}0]_{\text{TiB}_2} // [101]_{\text{Al}}$ ,  $(01\bar{1}0)_{\text{TiB}_2} // (11\bar{1})_{\text{Al}}$  (Fig. 5). Due to the introduction of IP, the crystallographic orientation relationships between TiB<sub>2</sub> particle and Al matrix changes. High resolution STEM-HAADF images (Fig. 5(a) and 5(c)) revealed the coherency evolution of the interfaces between TiB<sub>2</sub> and Al matrix before and after PA treatment. Formation of the TiB<sub>2</sub>/IP/Al sandwich structure through interfacial precipitation during the PA treatment significantly enhanced the TiB<sub>2</sub>/Al interface coherency. For example, the original TiB<sub>2</sub>/Al interface parallel to the prismatic  $\{01\bar{1}0\}_{\text{TiB}_2}$  facet shows a high mismatch of 38.03 % (Fig. 5(a) and 5(b)), while the newly formed TiB<sub>2</sub>/IP interface  $(01\bar{1}0)_{\text{TiB}_2} // (11\bar{2}8)_{\text{IP}}$  and IP/Al interface  $(11\bar{2}4)_{\text{IP}} // (11\bar{1})_{\text{Al}}$  show much lower mismatch values of 2.94 % and 0.08 %, respectively (Fig. 5(c) and 5(d)). Here, the calculation process of misfit dislocation interval is as follows. It assumes  $d_\alpha$  and  $d_\beta$  are the unstressed interplanar spacings of matching planes in the  $\alpha$  and  $\beta$  phases respectively, the mismatch  $\delta$  between the two lattices ( $d$ ) is defined by Eq. (2) [41]:

$$\delta = (d_\beta - d_\alpha)/d_\alpha \quad (2)$$

where the lattice misfit can be completely accommodated by a set of edge dislocations with a spacing  $D$  given by Eq. (3) [41]:

$$D = d_\beta/\delta. \quad (3)$$

Hence, take  $(01\bar{1}0)_{\text{TiB}_2}$  interface plane as an example. Where  $d_{\text{Al}} = 0.234$  nm,  $d_{\text{TiB}_2} = 0.323$  nm [42], the mismatch can be calculated to be  $\delta = (d_{\text{TiB}_2} - d_{\text{Al}})/d_{\text{Al}} \times 100\% = 38.03\%$ , while the misfit dislocation interval can be obtained as  $D = d_{\text{TiB}_2}/\delta = 0.85$  nm.

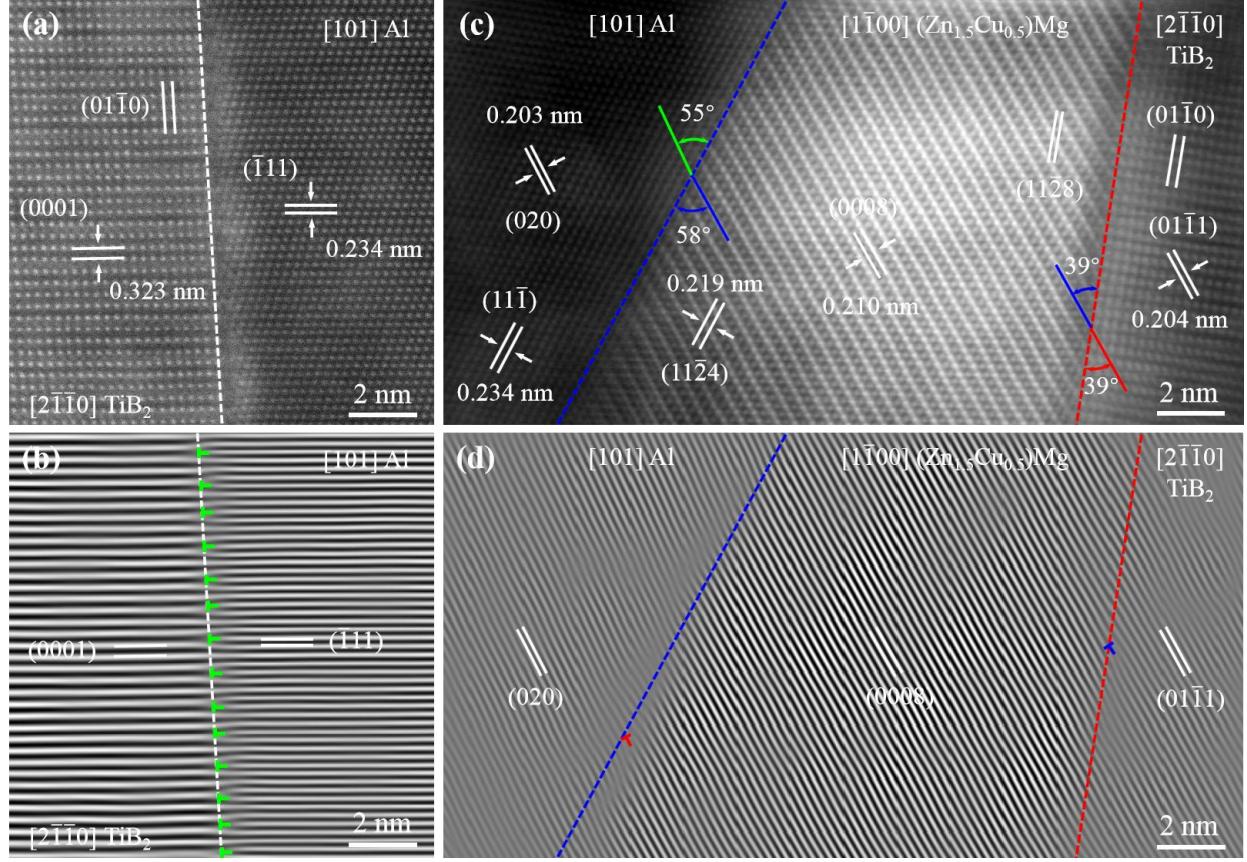


Fig. 5 Atomic structure of the representative  $\text{TiB}_2/\text{Al}$  interfaces and  $\text{TiB}_2/\text{Mg}(\text{Zn}_{1.5}\text{Cu}_{0.5})/\text{Al}$  multi-interfaces showing the interfacial coherency evolution. High resolution STEM-HAADF images of (a) the  $\text{TiB}_2/\text{Al}$  interface parallel to the prismatic  $\{01\bar{1}0\}$  facet and (c) the  $\text{TiB}_2/\text{Mg}(\text{Zn}_{1.5}\text{Cu}_{0.5})/\text{Al}$  multi-interfaces  $(01\bar{1}0)_{\text{TiB}_2} // (11\bar{2}8)_{\text{IP}}$  and  $(11\bar{2}4)_{\text{IP}} // (11\bar{1})_{\text{Al}}$ ; (b) and (d) are the corresponding IFFT images of (a) and (c), respectively, to highlight interface misfit dislocations and coherency. The projection axes are  $[2\bar{1}\bar{1}0]_{\text{TiB}_2} // [101]_{\text{Al}}$  and  $[1\bar{1}00]_{\text{IP}} // [2\bar{1}\bar{1}0]_{\text{TiB}_2} // [101]_{\text{Al}}$ , respectively.



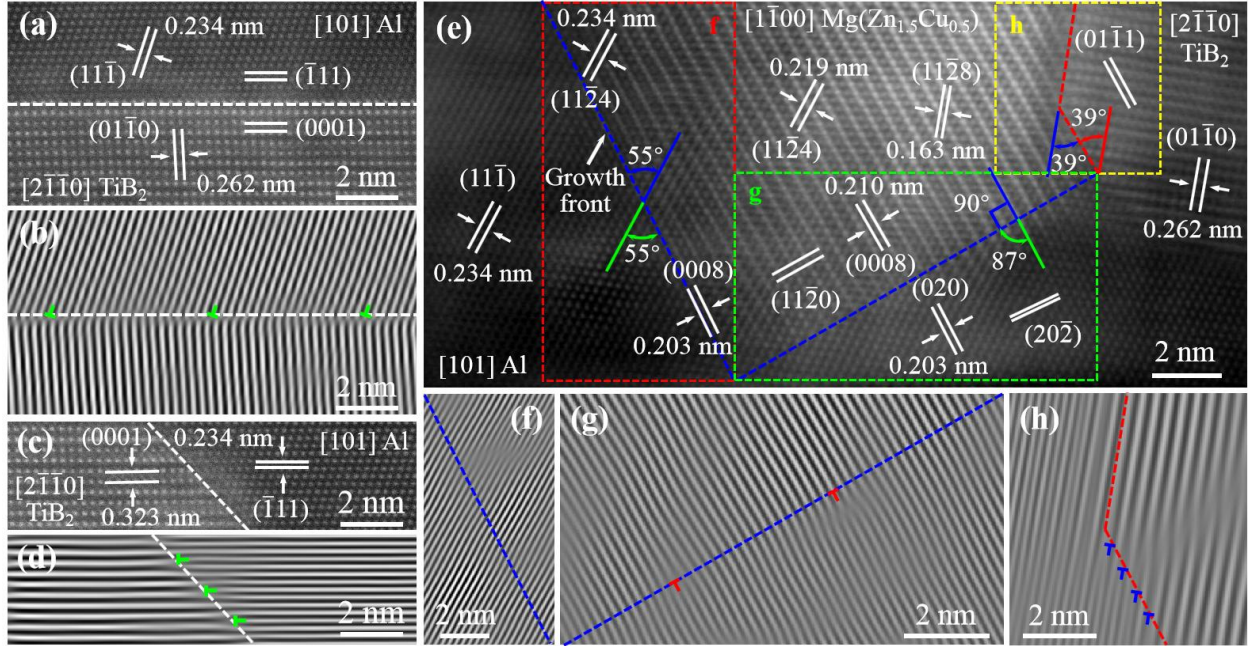


Fig. 6 Atomic structure of the rest of  $\text{TiB}_2/\text{Al}$  interfaces and  $\text{TiB}_2/\text{Mg}(\text{Zn}_{1.5}\text{Cu}_{0.5})/\text{Al}$  multi-interfaces showing the interfacial coherency evolution. High resolution STEM-HAADF images of the  $\text{TiB}_2/\text{Al}$  interface parallel to (a) the basal  $\{0001\}$  and (c) pyramidal  $\{01\bar{1}1\}$  facets of  $\text{TiB}_2$  nanoparticles; (b) and (d) are the corresponding IFFT images of (a) and (c), respectively, to highlight interface misfit dislocations. The projection direction is  $[2\bar{1}\bar{1}0]_{\text{TiB}_2} // [101]_{\text{Al}}$ . High resolution STEM-HAADF images of the  $\text{TiB}_2/\text{Mg}(\text{Zn}_{1.5}\text{Cu}_{0.5})/\text{Al}$  multi-interfaces, including the IP/Al interfaces  $(0008)_{\text{IP}} // (020)_{\text{Al}}$ ,  $(11\bar{2}0)_{\text{IP}} 3^\circ$  from  $(20\bar{2})_{\text{Al}}$ , and  $\text{TiB}_2/\text{IP}$  interface  $(01\bar{1}1)_{\text{TiB}_2} // (0008)_{\text{IP}}$ ; (f), (g) and (h) are the corresponding IFFT images of zoom-zone f, g and h, accordingly, to highlight interface misfit dislocations. The projection axis is  $[101]_{\text{Al}} // [1\bar{1}00]_{\text{IP}} // [2\bar{1}\bar{1}0]_{\text{TiB}_2}$ .

The interfacial coherency of the rest of  $\text{TiB}_2/\text{Al}$  interfaces is given in Fig. 6(a-d). For the  $\text{TiB}_2/\text{Al}$  interfaces parallel to the basal  $\{0001\}$  facets (Fig. 6(a)) and pyramidal  $\{01\bar{1}1\}$  facets (Fig. 6(c)) of  $\text{TiB}_2$  nanoparticles, the projected interplanar distances give a mismatch of 5.87 % and 38.03 %, respectively. The interfacial coherency of the rest of  $\text{TiB}_2/\text{Mg}(\text{Zn}_{1.5}\text{Cu}_{0.5})/\text{Al}$  multi-interfaces is given in Fig. 6(e-h). Notably, the atomic structure of the IP in the zone near growth front is slightly different from the typical structure of  $\text{Mg}(\text{Zn}_{1.5}\text{Cu}_{0.5})$  phase, i.e., shows a transition feature (Fig. 6(e)). From the growth front to the relatively early formed zone of the IP, the  $(0008)_{\text{IP}}$  plane gradually deviates up to  $3^\circ$  away from the initial direction being completely parallel to  $(020)_{\text{Al}}$ , while its interplanar spacing increases from 0.203 to 0.210 nm. Similar structure evolution of the  $(11\bar{2}4)_{\text{IP}}$  plane is also observed where its interplanar spacing decreases



from 0.234 to 0.219 nm. Here, it should be noted that the precipitation of  $(\text{Zn}_{1.5}\text{Cu}_{0.5})\text{Mg}$  interphase involves the formation of precipitates with a different composition compared to the Al alloy matrix, therefore long-range diffusion is required [41]. This is a continuous and time-consuming phase transformation process featured by thermally activated atomic movements [41, 43]. As such, a metastable transitional zone should exist at the growth front of interphase. Considering the  $(\text{Zn}_{1.5}\text{Cu}_{0.5})\text{Mg}$  interphase grew based on  $(0008)_{\text{IP}}$  planes along the growth direction  $\langle 0001 \rangle_{\text{IP}}$ , its growth front is  $(0008)_{\text{IP}} // (020)_{\text{Al}}$  interface planes. Hence, the atomic structure at the  $(0008)_{\text{IP}} // (020)_{\text{Al}}$  interface (i.e., the metastable transitional zone) is slightly different from the ones at the zones away from it (i.e., the stable zone). In this way, as is shown in Fig. 6, the interplanar spacings of  $(0008)_{\text{IP}}$  and  $(11\bar{2}4)_{\text{IP}}$  are 0.203 nm and 0.234 nm respectively at the  $(0008)_{\text{IP}} // (020)_{\text{Al}}$  interface (i.e., the metastable transitional zone), while the ones at the zones away from it (i.e., the stable zone) are 0.210 nm and 0.219 nm respectively, that is, the typical interplanar spacings of  $(\text{Zn}_{1.5}\text{Cu}_{0.5})\text{Mg}$  interphase. For the  $(0008)_{\text{IP}} // (020)_{\text{Al}}$  and  $(11\bar{2}4)_{\text{IP}} // (11\bar{1})_{\text{Al}}$  interface planes at the growth front of  $(\text{Zn}_{1.5}\text{Cu}_{0.5})\text{Mg}$  interphase, 0.203 nm and 0.234 nm are used to calculate the interface mismatch, while the typical 0.210 nm and 0.219 nm are used to calculate the interface mismatch of  $(0008)_{\text{IP}} // (020)_{\text{Al}}$  and  $(11\bar{2}4)_{\text{IP}} // (11\bar{1})_{\text{Al}}$  interface planes away from the growth front of  $(\text{Zn}_{1.5}\text{Cu}_{0.5})\text{Mg}$  interphase. The interface  $(0008)_{\text{IP}} // (020)_{\text{Al}}$  is thereby fully-coherent with no misfit dislocation observed (Fig. 6(f)), which is different from the theoretical mismatch value 6.85 %. For the other IP/Al interface  $(11\bar{2}0)_{\text{IP}} 3^\circ$  from  $(20\bar{2})_{\text{Al}}$ , the two observed misfit dislocations give a mismatch of 3.31 % (Fig. 6(g)). The IP/TiB<sub>2</sub> interface  $(0008)_{\text{IP}} // (01\bar{1}1)_{\text{TiB}_2}$  displays four misfit dislocations (Fig. 6(h)), suggesting that the observed IP was not directly nucleated at this interface considering the precipitation kinetics and the very high mismatch of 60.74 %. The detailed interface coherency results are summarized in Table 1.

Table 1 Coherency of the TiB<sub>2</sub>/Al interfaces and TiB<sub>2</sub>/Mg(Zn<sub>1.5</sub>Cu<sub>0.5</sub>)/Al multi-interfaces. Note that high, intermediate and low interface coherency are defined as the interface mismatch below 5%, in the range 5-25% and above 25%, respectively.

Samples	Interface type	Interface planes	Interface mismatch (%)	Misfit dislocation interval (nm)	Interface coherency
TiB <sub>2</sub> /7075Al-WQ	TiB <sub>2</sub> /Al	(0001) <sub>TiB<sub>2</sub></sub> // ( $\bar{1}$ 11) <sub>Al</sub>	5.87	4.15	Intermediate
		(01 $\bar{1}$ 0) <sub>TiB<sub>2</sub></sub>	38.03	0.85	Low
		(01 $\bar{1}$ 1) <sub>TiB<sub>2</sub></sub>	38.03	0.85	Low
TiB <sub>2</sub> /7075Al-PA	TiB <sub>2</sub> /Al	(0001) <sub>TiB<sub>2</sub></sub> // ( $\bar{1}$ 11) <sub>Al</sub>	5.87	4.15	Intermediate
		(11 $\bar{2}$ 4) <sub>IP</sub> // (11 $\bar{1}$ ) <sub>Al</sub>	0.08	322.99	High
	IP/Al	(0008) <sub>IP</sub> // (020) <sub>Al</sub>	0	--	High
		(11 $\bar{2}$ 0) <sub>IP</sub>	3.31	6.35	High
	TiB <sub>2</sub> /IP	(01 $\bar{1}$ 0) <sub>TiB<sub>2</sub></sub> // (11 $\bar{2}$ 8) <sub>IP</sub>	2.94	11.35	High
		(01 $\bar{1}$ 1) <sub>TiB<sub>2</sub></sub> // (0008) <sub>IP</sub>	60.74	0.68	Low

### 3.3 Mechanical properties and work hardening behavior

Room temperature tensile tests were carried out on the 7075Al-PA, TiB<sub>2</sub>/7075Al-WQ and TiB<sub>2</sub>/7075Al-PA samples, and compared with the commercial AA7075 Al alloys reported in Ref. [44] (Fig. 7). Our 7075Al-PA sample exhibits very similar stress-strain curve compared to that of the AA7075Al-PA sample in Ref. [44]. But, both the TiB<sub>2</sub>/7075Al-WQ and TiB<sub>2</sub>/7075Al-PA composite samples show higher yield stress and ultimate tensile strength (UTS) than their matrix counterparts, while maintaining a high uniform elongation (Table 2). For example, the yield stress and UTS of the AA7075Al-PA sample in Ref. [44] are respectively 452.3 MPa and 548.2 MPa, but they are increased to 610.5 MPa and 676.4 MPa in the composite with nearly the same uniform elongation values of around 12.0 % in both materials. Compared with the reported tensile properties of various Al-based materials (Fig. 7(b)), which generally show an inverse relationship between the strength and ductility, it is clear that our TiB<sub>2</sub>/7075Al-PA composite stands out from the trend showing the superior combination of strength and ductility. This demonstrates the success of our design strategy in breakthrough the strength-ductility trade-off. In addition, the large scale of the as-FSPed bulk samples (Fig. S1) indicates that the proposed processing processes are upscalable for removing the limit of sample size. Fig. 7(c) and 7(d) shows the fracture appearance of the 7075Al-PA and TiB<sub>2</sub>/7075Al-PA samples. The fracture

morphology is mainly dominated by fine and equiaxed dimples, indicating that the fracture process is mainly controlled by ductility behavior associated with dislocation activities.

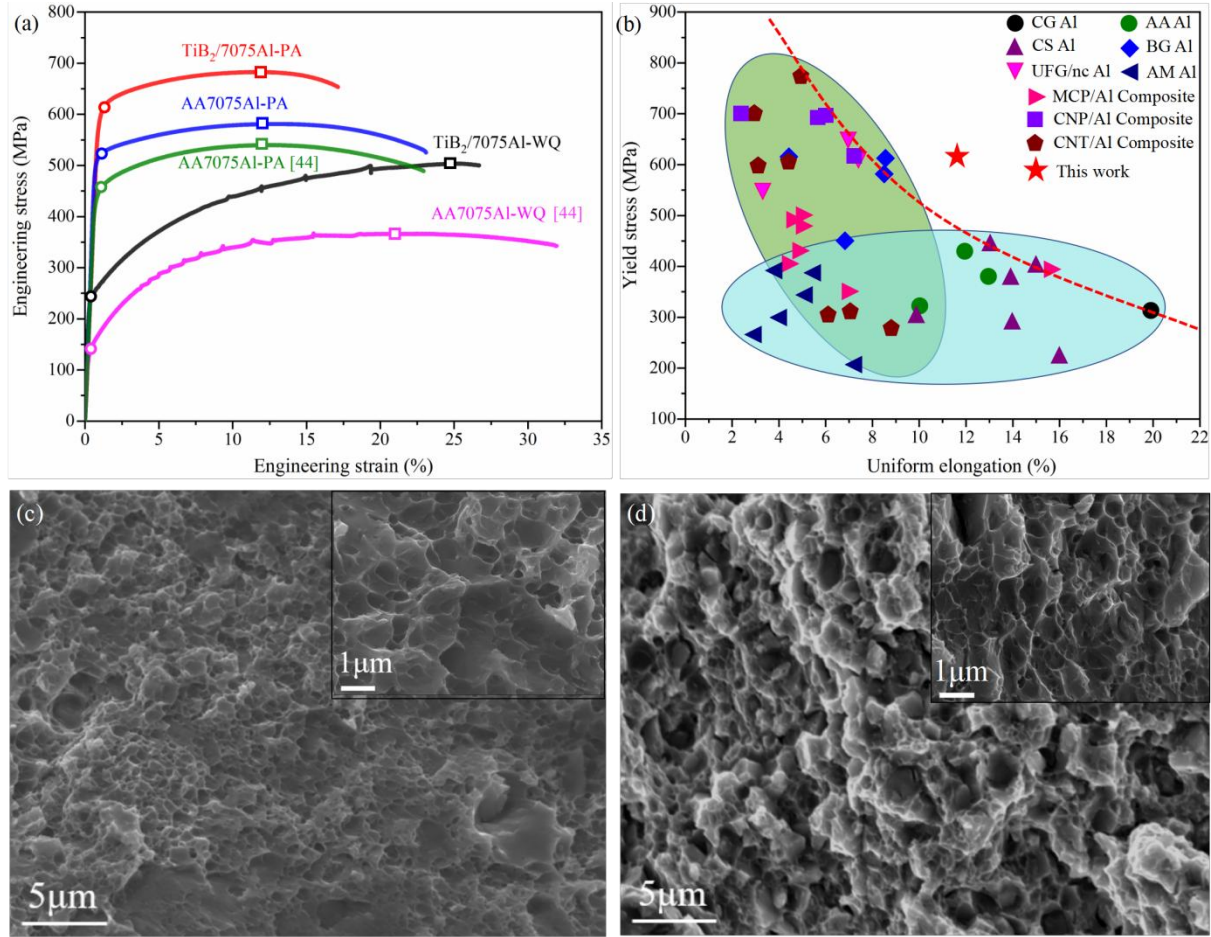


Fig. 7 Mechanical properties and the corresponding fracture appearance: (a) room-temperature tensile stress-strain curves of the TiB<sub>2</sub>/7075Al-WQ and TiB<sub>2</sub>/7075Al-PA composites and the commercial AA7075 Al alloys. The start of yield strength and the end of uniform elongation are marked by circles and hollow squares, respectively; (b) summary of yield stress versus uniform elongation of various Al materials, including coarse-grained Al alloys (CG Al) [45], commercial Al alloys (AA Al) [44], cyclic strengthening processed Al alloys (CS Al) [44], ultra-fine grained/nanocrystalline Al alloys (UFG/nc Al) [45,46], heterogeneous structure Al alloys (HS Al) [47,48], additively-manufactured Al alloys (AM Al) [49,50], micron or submicron scale ceramic particles reinforced Al alloys matrix composites (MCP/Al composites) [51,52], CNPs reinforced Al alloy matrix composites (CNP/Al composites) [53,54], carbon nanotube reinforced Al alloy matrix composites (CNT/Al composites) [47,55,56], and TiB<sub>2</sub>/7075Al composite (this work). The red dashed line approximately represents the boundary of strength-ductility; (c-d) fracture

appearance of 7075Al-PA and TiB<sub>2</sub>/7075Al-PA samples, and the inset images in (c) and (d) are corresponding high magnification images.

Table 2 Summary of yield stress, UTS and uniform elongation values determined from the tensile curves shown in Fig. 7.

Samples	Yield stress (MPa)	UTS (MPa)	Uniform elongation (%)
AA7075-WQ [44]	148.5 ± 6.4	375.0 ± 9.9	20.4 ± 1.2
AA7075-PA [44]	452.3 ± 22.5	548.2 ± 10.7	12.0 ± 0.7
TiB <sub>2</sub> /7075Al-WQ (This work)	277.0 ± 35.4	506.8 ± 4.7	23.1 ± 2.9
TiB <sub>2</sub> /7075Al-PA (This work)	610.5 ± 6.4	676.4 ± 5.8	11.5 ± 0.2

The evolution of dislocation density,  $\rho$ , during tensile deformation can be described by using Kocks-Mecking model [57]:

$$d\rho / d\varepsilon = k_1 \sqrt{\rho} - k_2 \rho \quad (4)$$

where  $k_1$  is a constant that represents the dislocation storage due to dislocation-dislocation interaction;  $k_2$  represents a reduction in dislocation caused by dynamic recovery. The flow stress due to the variation of dislocation density (i.e. dislocation strengthening),  $\sigma_{ds}$ , during tensile deformation can be denoted using the Taylor equation [58]:

$$\sigma_{ds} = \alpha G b M \sqrt{\rho} \quad (5)$$

where  $\alpha$  is a constant,  $\alpha = 0.2$  [59];  $G$  is the Shear modulus,  $G = 26.9$  GPa for 7075 Al [59];  $b$  is the Burgers vector,  $b = 0.286$  nm for face-centered cubic (FCC) Al;  $M$  is the Taylor factor,  $M=3.06$  for FCC polycrystalline matrix. The well-known Voce equation is used to establish the relationship between  $\sigma_{ds}$  and plastic strain  $\varepsilon^p$  [60]:

$$\sigma_{ds} = \sigma^S - \sigma^S \exp \left[ -(\theta_0 / \sigma^S) \cdot \varepsilon^p \right] \quad (6)$$

where  $\sigma^S$  is the saturated stress,  $\sigma^S = \alpha G b M k_1 / k_2$ . It should be noted that the total flow stress  $\sigma_{total}$  is consisted of dislocation strengthening and other strengthening (such as solution concentration, grain boundary strengthening and particle strengthening). During tensile deformation, the dislocation strengthening depends on strain accumulation, and the other strengthening can be regarded as constant. Therefore, the work hardening rate,  $\theta$ , is denoted based on Eqs. (4), (5) and (6)

$$\theta = d\sigma_{total} / d\varepsilon^p = d\sigma_{ds} / d\varepsilon^p = \theta_0 (1 - \sigma_{ds} / \sigma^S) \quad (7)$$

where  $\theta_0$  is the initial work hardening rate,  $\theta_0 = aGb k_1 M^2 / 2$ . After differentiating with  $\sigma_{total}$ , it obtains:

$$\theta / \sigma_{total} = \theta / \sigma_{ds} = M k_2 / 2 \quad (8)$$

where it can be inferred that the slope of work hardening rate versus flow stress (Fig. 8(a) and 8(b)) represents the dislocation dynamic recovery rate. The work hardening rate of the TiB<sub>2</sub>/7075-PA composite is higher than 7075Al-PA, and a higher **slope** on the work hardening rate curves is obtained in the TiB<sub>2</sub>/7075-PA composite than the 7075-PA alloy (Fig. 8(b)). Since the curve **slope** represents the dynamic recovery rate of dislocation according to theory described by Eqs. (4-8) and the values of  $k_2$  of the 7075Al-PA, TiB<sub>2</sub>/7075-WQ and TiB<sub>2</sub>/7075-PA are 7.54, 5.75 and 14.29; respectively. The value of  $k_2$  of the TiB<sub>2</sub>/7075-PA sample is much higher than the 7075Al-PA and TiB<sub>2</sub>/7075-WQ samples, indicating that the dislocation dynamic recovery rate of the TiB<sub>2</sub>/7075-PA sample is much higher than the other two samples.

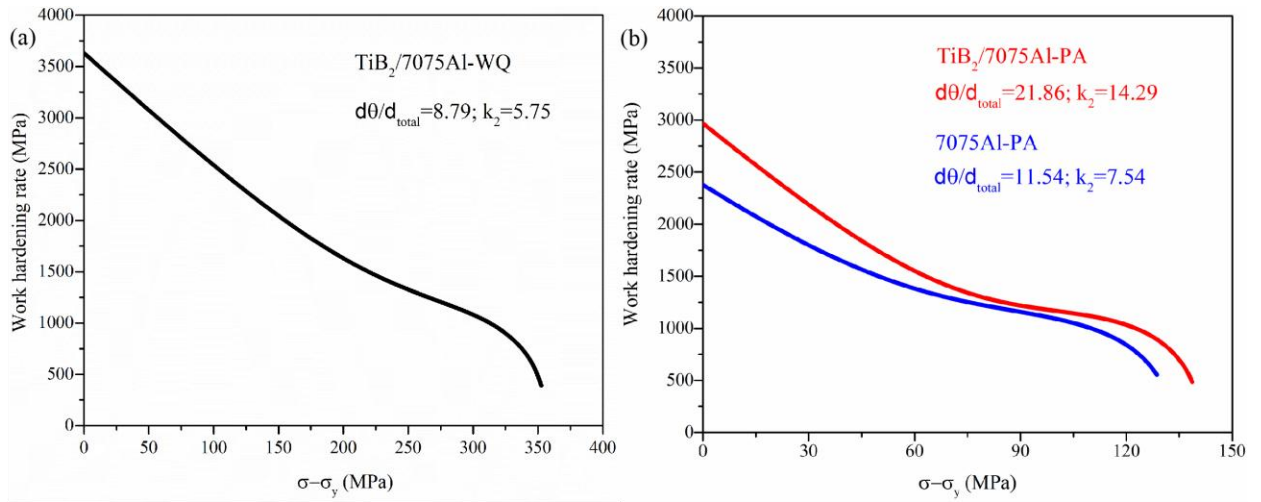


Fig. 8 Variation of work hardening rate versus flow stress with yield stress subtracted for (a) TiB<sub>2</sub>/7075Al-WQ, (b) 7075Al-PA and TiB<sub>2</sub>/7075-PA samples

## 4. Discussion

### 4.1 Utilizing IP for improving interface coherency and interface strength

The precipitation behavior during PA is influenced due to the existence of high misfit TiB<sub>2</sub>/Al interfaces in the TiB<sub>2</sub>/7075Al-WQ composite. On the one hand, the TiB<sub>2</sub>/Al interfaces can be preferred sites for promoting the heterogeneous precipitation, since the energy barrier for the heterogeneous precipitations at the TiB<sub>2</sub>/Al interfaces reduces compared with the

homogeneous nucleation in the Al matrix away from the interface [41]. On the other hand, the stress field induced by highly-dense misfit dislocations at the  $\text{TiB}_2/\text{Al}$  interfaces could provide the driving force for the migration of solute atoms and vacancies to interface, which is beneficial for the nucleation of the IP at the  $\text{TiB}_2/\text{Al}$  interfaces [61,62]. Therefore, due to the above two reasons, the IP occurs at the  $\text{TiB}_2/\text{Al}$  interfaces during PA.

Our results show that the interface coherency is improved due to the introduction of IP (Figs. 5 and 6, Table 1). Here, the E2EM model was applied to calculate the mismatches, and therefore to predict orientation relationships between phases in the  $\text{TiB}_2/\text{IP}/\text{Al}$  sandwich structure. From the powder diffraction file database [42], Al has a simple FCC lattice structure with  $a = 0.40494$  nm;  $\text{TiB}_2$  has a simple hexagonal lattice structure with  $a = 0.3038$  nm and  $c = 0.3262$  nm and belongs to  $P6/mmm$  space group. The  $\text{Mg}(\text{Zn}_{1.5}\text{Cu}_{0.5})$  also has an hexagonal lattice structure with lattice parameters  $a = 0.5124$  nm and  $c = 1.682$  nm and space group of  $P6_3/mmc$ . Each unit cell contains 12 Zn atoms, 8 Mg atoms and 4 Cu atoms. Based the crystallographic data, the crystallography of the  $\text{TiB}_2$  nanoparticle, 7075Al matrix and the  $\text{Mg}(\text{Zn}_{1.5}\text{Cu}_{0.5})$  formed in between is predicted [33,63]. Fig. 9 shows the predicted orientation relationships (expressed by one direction parallelism and one plane pair) and the calculated misfits along the matching directions and mismatches between the matching planes among  $\text{TiB}_2$ , IP and  $\alpha\text{-Al}$  phases. The blue bars within the triangle indicate values of mismatch between the matching planes, which is accommodated by a rotation of one of matching planes about the matching direction. Green bars outside of the triangle show the misfits along various matching directions, which defines the maximum size of particles to retain coherency with the matrix. Lower misfit values along the matching directions between  $\text{TiB}_2/\text{Al}$  and IP than that between the Al and  $\text{TiB}_2$  imply the preference of the formation of IP in between the Al and  $\text{TiB}_2$ . The result in Fig. 9 further demonstrates that the interface coherency of  $\text{TiB}_2/\text{Al}$  interfaces is improved due to the introduction of IP, which agrees well with the experimental results shown in Figs. 5 and 6 as well as Table 1.



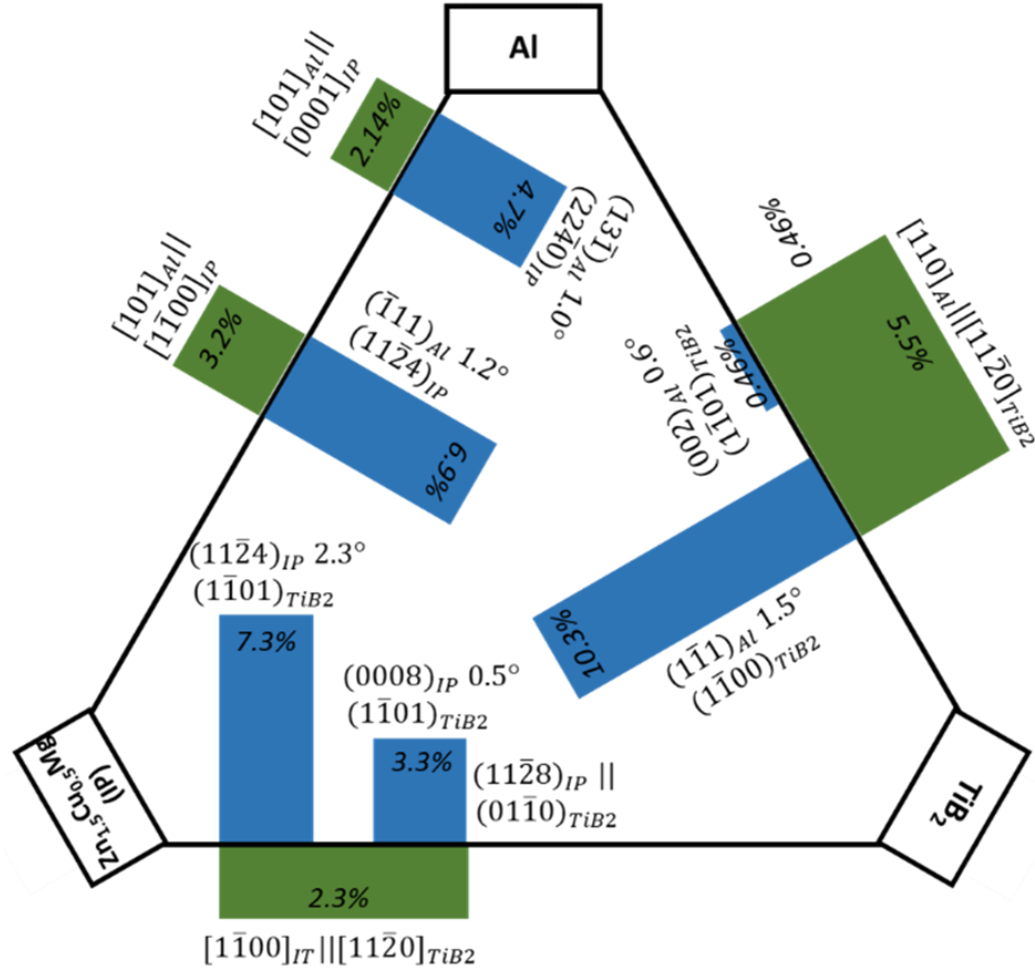


Fig. 9 Calculated values of misfit along matching directions and mismatch between matching plane among Al, TiB<sub>2</sub> and IP using the E2EM model.

Further, the first-principles calculations in Fig. 10 are used to illustrate that the interface strength increases along with the interface coherency. It was used to bridge the gap between the above-mentioned interface coherency and interface strength being unachievable experimentally. For example, considering the mismatch value of the TiB<sub>2</sub>/Al interface of 38.03 % in the TiB<sub>2</sub>/7075Al-WQ sample (Table 1), such an interface was treated as constrained with Al lattice constants. Thus, the calculated works of adhesion ( $W_{ad}$ ) are 2.9356 J/m<sup>2</sup> for B-terminated (case No. 1) and 2.0706 J/m<sup>2</sup> for Ti-terminated interfaces (case No. 2). It is observed from the atomic snapshots that Al atoms in B-terminated interface are relocated, making a stronger interface compared with Ti-terminated one. Comparatively, the mismatch value of the Al/IP interface is as low as 0.08 % in TiB<sub>2</sub>/7075Al-PA sample. Thus, the calculated  $W_{ad}$  of this interface with different lattice constraints is within 2.237 ~ 1.9194 J/m<sup>2</sup>. As shown by the atomic snapshots in

the cases No. 3 and 4, the movement of Al atoms at the interfaces is limited after relaxation. Regarding the IP/TiB<sub>2</sub> interface, the observed mismatch value is 2.94 %, higher than the Al/IP interface while much lower than the initial TiB<sub>2</sub>/Al interface. The calculated  $W_{ad}$  of the IP/TiB<sub>2</sub> interface is diverged using different terminations. For example, the  $W_{ad}$  of the Ti-terminated TiB<sub>2</sub> interface with Cu-segregated IP is just 2.0779 J/m<sup>2</sup> (case No. 5), almost the same as with the Ti-terminated TiB<sub>2</sub>/Al interface. However, the  $W_{ad}$  of the B-terminated TiB<sub>2</sub> interface with Cu-segregated IP is 3.8412 J/m<sup>2</sup>, the largest value obtained in the present calculations (case No. 6). The corresponding atomic snapshots of the cases Nos. 5 and 6 also show that just like the B-terminated TiB<sub>2</sub>/Al interface, relocated metal atoms in the interface area make the strongest interface among all the investigated interfaces. Furthermore, to clarify the role of different elements to the interface strength, the interactions between Al and other element atoms were calculated with dimers method and shown in Fig. 10(c). From Fig. 10(c), one can find that Al/TiB<sub>2</sub> interface should much stronger than Al/MgZn<sub>2</sub> interface, and only after Cu atoms solute into MgZn<sub>2</sub> to form Mg(Zn<sub>1.5</sub>Cu<sub>0.5</sub>), it is possible to form stronger interface than Al/TiB<sub>2</sub>. In short summary, although the calculated  $W_{ad}$  is dependent on the interface termination, the general trend is that the higher interface coherency and the higher interface strength, and Cu segregation facilitates interface strength.



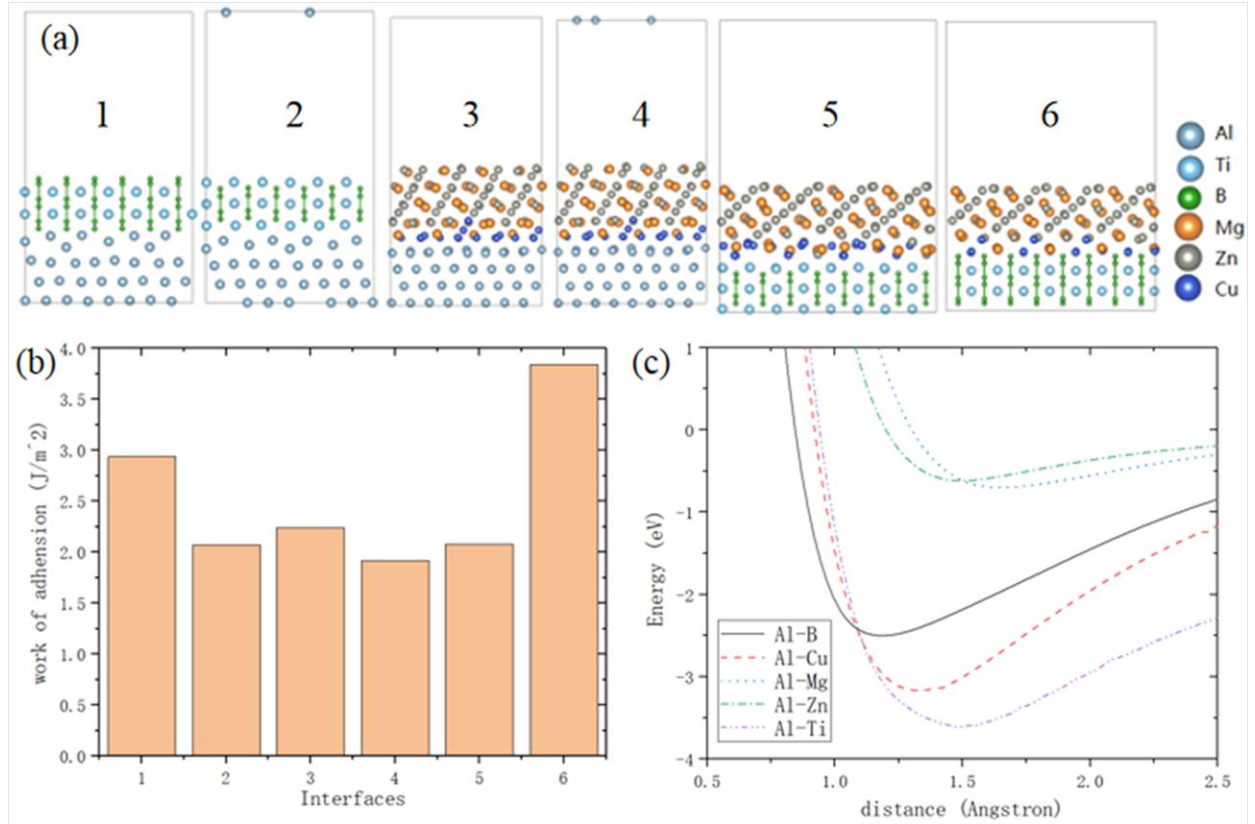


Fig. 10 (a) DFT relaxed interface models of the different  $\text{TiB}_2/\text{Al}$  and  $\text{TiB}_2/\text{IP}/\text{Al}$  interfaces (case No. 1-6); (b) calculated work of adhesion ( $W_{ad}$ ) of case No. 1-6 (Data are listed in Table S1), and (c) interaction between Al-X dimers

### 4.3 Strengthening mechanisms

Comparing with the unreinforced 7075Al counterpart, the possible factors contributing to the strengthening increments in the  $\text{TiB}_2/7075\text{Al-WQ}$  and  $\text{TiB}_2/7075\text{Al-PA}$  composites are caused by dislocation, precipitation, grain boundary, Orowan and load-bearing strengthening mechanisms. The contributions to yield strength caused by above strengthening mechanisms are discussed as follows:

#### (1) Dislocation strengthening

The dislocation densities in the  $\text{TiB}_2/7075\text{Al-WQ}$  and  $\text{TiB}_2/7075\text{Al-PA}$  samples before tensile deformation are measured using SRXRD (Fig. S2), which are about  $6.1 \times 10^{13} \text{ m}^{-2}$  and  $5.1 \times 10^{13} \text{ m}^{-2}$ ; respectively. The dislocation strengthening increment,  $\sigma_{ds}$ , in both samples can be

estimated by using the Taylor equation (Eq. (5)). The values of  $\sigma_{ds}$  in the TiB<sub>2</sub>/7075Al-WQ and TiB<sub>2</sub>/7075Al-PA samples are estimated as 12 and 11 MPa; respectively (Table 4).

## (2) Grain-boundary strengthening

The average grain size considering the three directions for the TiB<sub>2</sub>/7075Al-PA sample is about 2.72  $\mu\text{m}$  (Fig. 1). Here, the Hall-Petch equation is used to estimate the grain-boundary strengthening,  $\sigma_{gs}$ , as given by [64,65]:

$$\sigma_{gs} = k d^{-1/2} \quad (9)$$

where  $k$  is Hall-Petch coefficient,  $k = 0.12 \text{ MPa}\sqrt{m}$  for 7075 Al [59];  $d$  is the average grain size,  $d = 2.72 \mu\text{m}$ . Since the grain size in TiB<sub>2</sub>/7075Al-WQ sample is almost same compared with TiB<sub>2</sub>/7075Al-PA. Thus, both the values of  $\sigma_{gs}$  for TiB<sub>2</sub>/7075Al-WQ and TiB<sub>2</sub>/7075Al-PA samples are considered as 72.8 MPa (Table 4).

## (3) Solution strengthening

For the TiB<sub>2</sub>/7075Al-WQ sample, Zn, Mg and Cu solute atoms in the sample can promote the solution strengthening. The solution strengthening,  $\sigma_{ss}$ , is governed by the Fleischer equation, as given by [66]:

$$\sigma_{ss} = M G b \varepsilon_{ss}^{2/3} \sqrt{c} \quad (10)$$

where  $\varepsilon_{ss}$  refers to the lattice strain due to the difference in atom size between the solute and solvent, and the values are different for Zn, Mg and Cu (Table 3);  $c$  is the solute concentration in the matrix. From Table 3, the contribution to yield strength caused by Zn, Mg and Cu is about 20.0, 42.8 and 33.1 MPa, respectively. The total solution concentration caused by these three elements is about 95.9 MPa. For the TiB<sub>2</sub>/7075Al-PA sample, the solute concentrations of Zn, Mg and Cu in the matrix are very low, since the precipitation of GP zones and  $\eta'$  during PA decreases the solute concentration dramatically [67]. For simplicity, we do not consider the solution strengthening in the TiB<sub>2</sub>/7075Al-PA sample (Table 4).

Table 3 Parameters used for calculating the solution strengthening caused by Zn, Mg and Cu. Here  $R_{\text{das}}$  refers to the difference in atomic radii between Al and other elements;  $\sigma_{\text{ysi}}$  is the yield strength increment per weight percent;  $\sigma_{\text{tys}}$  is the total contribution to yield stress due to solution strengthening.

Elements	$R_{\text{das}}$ (%) [59]	$\sigma_{\text{ysi}}$ (MPa/wt%) [59]	$c$ (wt%)	$\sigma_{\text{tys}}$ (MPa)
Zn	-6	2.9	6.9	20.0

Mg	11.8	18.6	2.3	42.8
Cu	-10.7	13.8	2.4	33.1

#### (4) Particle strengthening

The main particles are  $\text{TiB}_2$  in the  $\text{TiB}_2/7075\text{Al-WQ}$  sample, and particle strengthening mechanism caused by  $\text{TiB}_2$  particles is Orowan bypassing mechanism. The Orowan strengthening increment caused by  $\text{TiB}_2$ ,  $\sigma_{ob}$ , is given as [59,68]:

$$\sigma_{ob} = M \frac{0.4 G b}{\pi \sqrt{1-\nu}} \frac{\ln(2\bar{r}/b)}{\lambda_p} \quad (11)$$

where  $\bar{r}$  is the mean radius of a circular cross-section in a random plane of particle,  $\bar{r} = \sqrt{2/3}r$ , where  $r$  is the mean radius of the particles,  $r = 49.2$  nm [38];  $\nu$  is the Poisson's ratio,  $\nu = 0.33$  for 7075 Al [59];  $\lambda_p$  is particle spacing and can be denoted as  $\lambda_p = 2\bar{r}(\sqrt{\pi/4f} - 1)$  [59,68], where  $f$  is the volume fraction of  $\text{TiB}_2$  particles and  $f = 0.022$ . Thus, the value of particle strengthening increment  $\sigma_{ps}$  is the value of  $\sigma_{ob}$  for  $\text{TiB}_2/7075\text{Al-WQ}$  sample, and this value is about 51.7 MPa according to Eq. (11) (Table 4).

However, the particle strengthening increment are caused by both  $\text{TiB}_2$  and precipitates (GP zones and  $\eta'$ ) in the  $\text{TiB}_2/7075\text{Al-PA}$  sample (Fig. 2(d) and 2(e)). The particle strengthening increment caused by  $\text{TiB}_2$  is the same as in the  $\text{TiB}_2/7075\text{Al-WQ}$  sample, since the characteristics of  $\text{TiB}_2$  particles can be assumed to be very similar in both samples. According to the previous studies, particle strengthening caused by GP zones and  $\eta'$  is governed by Orowan bypassing mechanism or shearing mechanism, and the one causing a smaller strengthening increment is the operative mechanism [59,68]. The shearing mechanism mainly contains coherency strengthening, modulus mismatch strengthening and order strengthening, which are denoted as [59,68-71]:

$$\sigma_{cs} = M a_\varepsilon (G \varepsilon_c)^{3/2} \left( \frac{rf}{0.5 G b} \right)^{1/2} \quad (12)$$

$$\sigma_{ms} = M 0.0055 (\Delta G)^{3/2} \left( \frac{2f}{G} \right)^{1/2} \left( \frac{r}{b} \right)^{3m/2-1} \quad (13)$$

$$\sigma_{os} = M 0.81 \frac{\gamma_{apb}}{2b} \left( \frac{3\pi f}{8} \right)^{1/2} \quad (14)$$

where  $a_\varepsilon$  is a constant,  $a_\varepsilon = 2.6$  for FCC metals [59];  $\varepsilon_c$  is the constrained lattice parameter misfit,  $\varepsilon_c = 0.3$  for 7075 Al [59].  $\Delta G$  is the different on shear modulus between precipitates ( $G_p = 25$  GPa [72]) and matrix ( $G_m = 26.9$  GPa [59]),  $\Delta G = 1.9$  GPa;  $m$  is a constant,  $m = 0.85$  [59];  $\gamma_{apb}$  is the antiphase boundary energy of the precipitates,  $\gamma_{apb} = 0.183$  J/m<sup>2</sup> [73]. The dominant shearing strengthening mechanism depends on the larger values of  $\sqrt{\sigma_{cs}^2 + \sigma_{ms}^2}$  and  $\sigma_{os}$  [59]. The Orowan bypassing mechanism caused by precipitates (GP zones and  $\eta'$ ) is also determined by Eq. (11). Thus, the particle strengthening caused by precipitates,  $\sigma_{ps}$ , is given as:

$$\sigma_{ps} = \text{small} \left\{ \text{large} \left( \sqrt{\sigma_{cs}^2 + \sigma_{ms}^2}, \sigma_{os} \right), \sigma_{ob} \right\}. \quad (15)$$

Here we use the values of 2.81 (the value of  $r$ ) and 1.41% (the value of  $f$ ) to estimate the particle strengthening increment caused by precipitates. The values of  $\sqrt{\sigma_{cs}^2 + \sigma_{ms}^2}$ ,  $\sigma_{os}$  and  $\sigma_{ob}$  caused by precipitates are about 18.5 GPa, 102.2 MPa, 342.4 MPa; respectively. Thus, the particle strengthening caused by precipitates is 342.4 MPa and the operative particle strengthening is Orowan strengthening. The total particle strengthening caused by both TiB<sub>2</sub> and precipitates (GP zones and  $\eta'$ ) is 394.1 MPa.

### (5) Load-bearing strengthening

Since both TiB<sub>2</sub>/7075Al-WQ and TiB<sub>2</sub>/7075Al-PA samples contain the TiB<sub>2</sub> ceramic particles as the reinforcement phase, it should consider the load-bearing strengthening,  $\sigma_{ls}$ , caused by the TiB<sub>2</sub> particles as given by [74]:

$$\sigma_{ls} = 1.5 f \sigma_i \quad (16)$$

where  $\sigma_i$  is the interfacial bonding strength;  $\sigma_i$  refers to the interface strength of TiB<sub>2</sub>/Al in the TiB<sub>2</sub>/7075Al-WQ sample and that of the TiB<sub>2</sub>/IP/Al multi-interfaces in the TiB<sub>2</sub>/7075Al-PA sample. However, it is only known qualitatively that the interface strength of TiB<sub>2</sub>/IP/Al enhances from the first-principles calculations (Fig. 10), and no approximate values on interface strength of TiB<sub>2</sub>/IP/Al multi-interfaces can be referenced from the existing studies. Thus, it is difficult to estimate the load-bearing strengthening increment  $\sigma_{ls}$  caused by TiB<sub>2</sub> particles in the TiB<sub>2</sub>/7075Al-PA sample according to Eq. (16). Based on the above analysis, the total yield strength can be estimated as:

$$\sigma_{\text{total}} = \sigma_0 + \sigma_{ds} + \sigma_{gs} + \sigma_{ss} + \sigma_{ps} + \sigma_{ls} \quad (17)$$

where  $\sigma_0$  is the friction stress,  $\sigma_0=20$  MPa [75].

In Table 4, it can be easily back-calculated from the experimental yield stress value that the values of  $\sigma_{ls}$  in the TiB<sub>2</sub>/7075Al-WQ and TiB<sub>2</sub>/7075Al-PA samples are about 24.6 and 112.6 MPa, respectively. The value of  $\sigma_{ls}$  in TiB<sub>2</sub>/7075Al-PA sample is nearly fivefold higher than in the TiB<sub>2</sub>/7075Al-WQ sample. It is indicated that the strengthening increment due to load-bearing strengthening mechanism increases significantly when the TiB<sub>2</sub>/IP/Al multi-interface forms.

Table 4 Different strengthening increments in the TiB<sub>2</sub>/7075Al-WQ and TiB<sub>2</sub>/7075Al-PA samples

Samples	$\sigma_0$	$\sigma_{ds}$	$\sigma_{gs}$	$\sigma_{ss}$	$\sigma_{ps}$	$\sigma_{ls}$	$\sigma_{total}$	Experiments
TiB <sub>2</sub> /7075Al-WQ	20	12	72.8	95.9	51.7	24.6	-	277.0
TiB <sub>2</sub> /7075Al-PA	20	11	72.8	-	394.1	112.6	-	610.5

#### 4.3 Mechanisms accounting for the extraordinary ductility

The Considere criterion describes that the plastic instability occurs when the work hardening rate is below the true flow stress. The normalized **work hardening rate** is expressed as:

$$\Theta = (1 / \sigma) \cdot \partial \sigma / \partial \varepsilon \quad (18)$$

where  $\sigma$  is the true flow stress and  $\varepsilon$  is the true strain. The plastic instability (i.e. necking) appears when the normalized **work hardening rate**  $\Theta \leq 1$ . Apparently, to stabilize the uniform tensile plastic deformation before necking,  $\Theta$  has to stay high enough to match with the increased stress  $\sigma$  avert the instability. A high **work hardening rate**, i.e., the continuous storage and multiplication of dislocations during plastic deformation, is thereby the key factor to acquire high ductility [76].



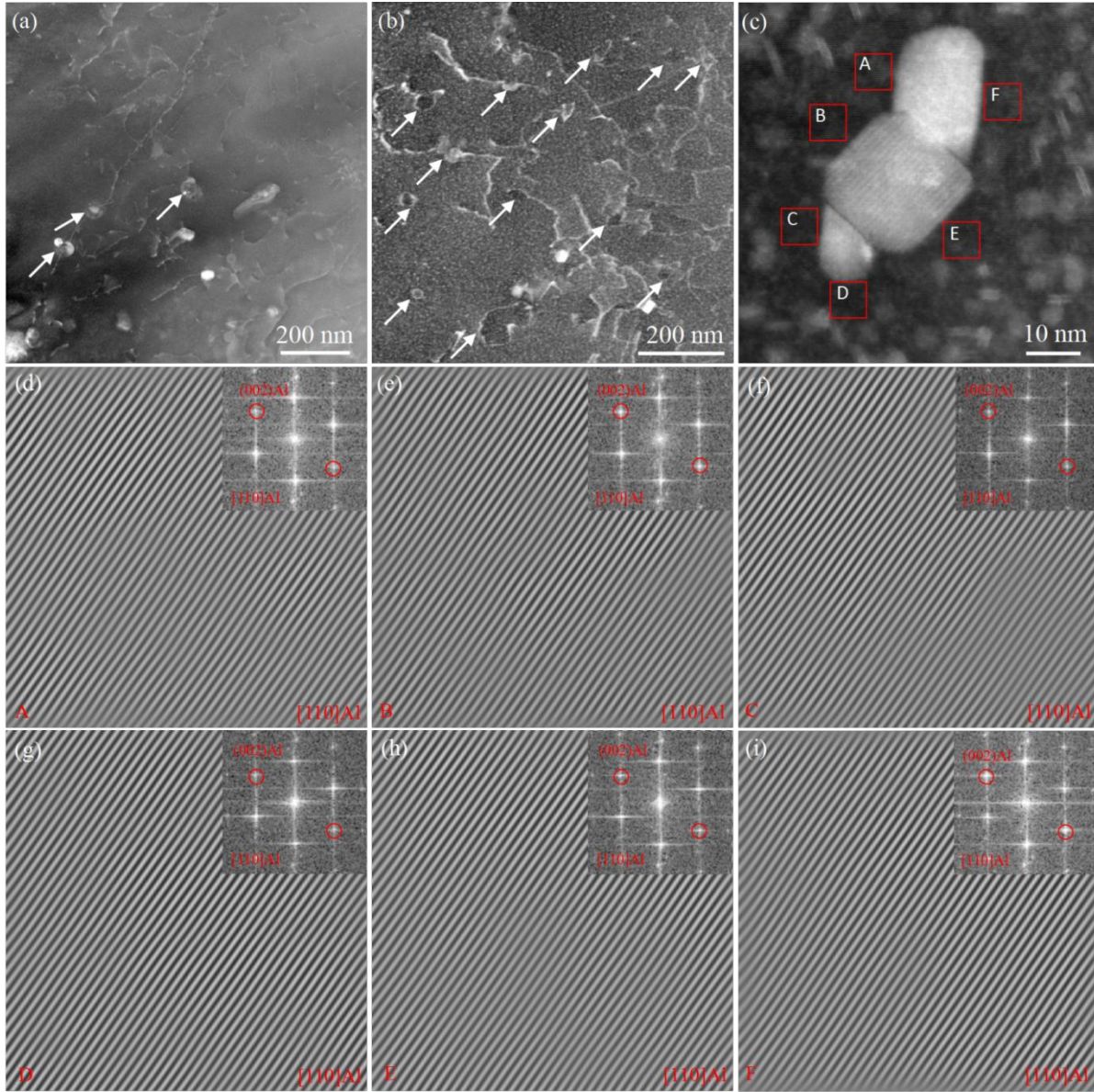


Fig. 11 STEM-HAADF images showing the dislocations of  $\text{TiB}_2/\text{7075Al-WQ}$  and  $\text{TiB}_2/\text{7075Al-PA}$  samples after 1.5% tensile strain: (a)  $\text{TiB}_2/\text{7075Al-WQ}$  sample; (b)  $\text{TiB}_2/\text{7075Al-PA}$  sample; (c) the  $\text{TiB}_2/\text{IP}/\text{Al}$  sandwich structure of  $\text{TiB}_2/\text{7075Al-PA}$  sample; (d-i) the IFFT images of six A, B, C, D, E and F red areas in (c) with reflection pairs selected in corresponding FFT patterns in insets. The white arrows in (a) and (b) are Orowan loops.

Fig. 11 shows the dislocations of the  $\text{TiB}_2/\text{7075Al-WQ}$  and  $\text{TiB}_2/\text{7075Al-PA}$  samples as well as the dislocation structure of a typical  $\text{TiB}_2/\text{IP}/\text{Al}$  interface after 1.5% tensile strain. It is shown that lots of Orowan loops (white arrows) form after deformation (Fig. 11(a) and 11(b)), but the number of Orowan loops in  $\text{TiB}_2/\text{7075Al-PA}$  is higher than  $\text{TiB}_2/\text{7075Al-WQ}$  sample.

Fig. 11(c-i) shows the the IFFT images of the selected areas next to the interface, and no dislocations are observed from the six areas, indicating that no evident dislocation pile-ups at the IP/Al and  $\text{TiB}_2/\text{Al}$  interfaces during deformation. Fig. S3 also shows the IFFT images of these six areas with other reflection pairs, and no dislocations are observed at the IP/Al and  $\text{TiB}_2/\text{Al}$  interfaces.

The influence of  $\text{TiB}_2/\text{IP}/\text{Al}$  interface on dislocation motion mode is illustrated in Fig. 12. Fig. 12(a) and 12(b) schematically show that the  $\text{TiB}_2/\text{Al}$  interface is modified due to the appearance of IP. Fig. 12(c) and 12(d) show the dislocation structure evolution at CNP/Al and CNP/IP/Al interfaces during tensile deformation. The dislocation multiplication and motion in the matrix at the beginning of plastic deformation occurs in both cases. When encountering CNPs, although some gliding dislocations can form Orowan loops surrounding the CNPs, lots of dislocations are trapped by the  $\text{TiB}_2/\text{Al}$  interfaces (Fig. 12(c)). While for CNP/IP/Al interfaces, most gliding dislocations form Orowan loops surrounding the CNPs, and fewer dislocations are trapped by the CNP/IP/Al interfaces (Fig. 12(d)). It is because that the interfaces with higher misfit exhibit lower shear resistance than the ones with lower misfit, since the intersections of misfit dislocations can act as preferred sites to form interface dislocation loop [77,78]. Thus, the lattice dislocations from the matrix will be attracted by the interface dislocations when the interface shears to response to the stress fields nearby the lattice dislocations. When the absorbed dislocations are across the interface, they can re-nucleate and bow out onto the outgoing slip systems. As this process needs thermal activation, it is usually hard to occur [77]. Therefore, more numbers of Orowan loops form within CNP/IP/Al interfaces in the  $\text{TiB}_2/7075\text{Al-PA}$  sample. This explains why no dislocations are observed at the  $\text{TiB}_2/\text{IP}/\text{Al}$  interfaces in the present work (Fig. 11(c-i) and Fig. S3)

With the increase in plastic deformation, both the accumulated Orowan loops and the piled-up dislocations appear at the CNP/Al interface (Fig. 12(c)). Previous studies showed that dislocations are prone to pile up at high misfit interfaces between particles and matrix [46,77-79]. Since these piled-up dislocations are not recovery and not easy to transmit across, the dislocation saturates quickly, reducing the work hardening rate. Furthermore, trapping of dislocations at interface limits the number of Orowan loops (Fig. 11(a)). Thus, strain localization takes place at the interfaces when the piled-up dislocations at CNP/Al interface reach a certain of level, advancing the appearance of plastic instability (Fig. 12(c)) and lowering ductility.

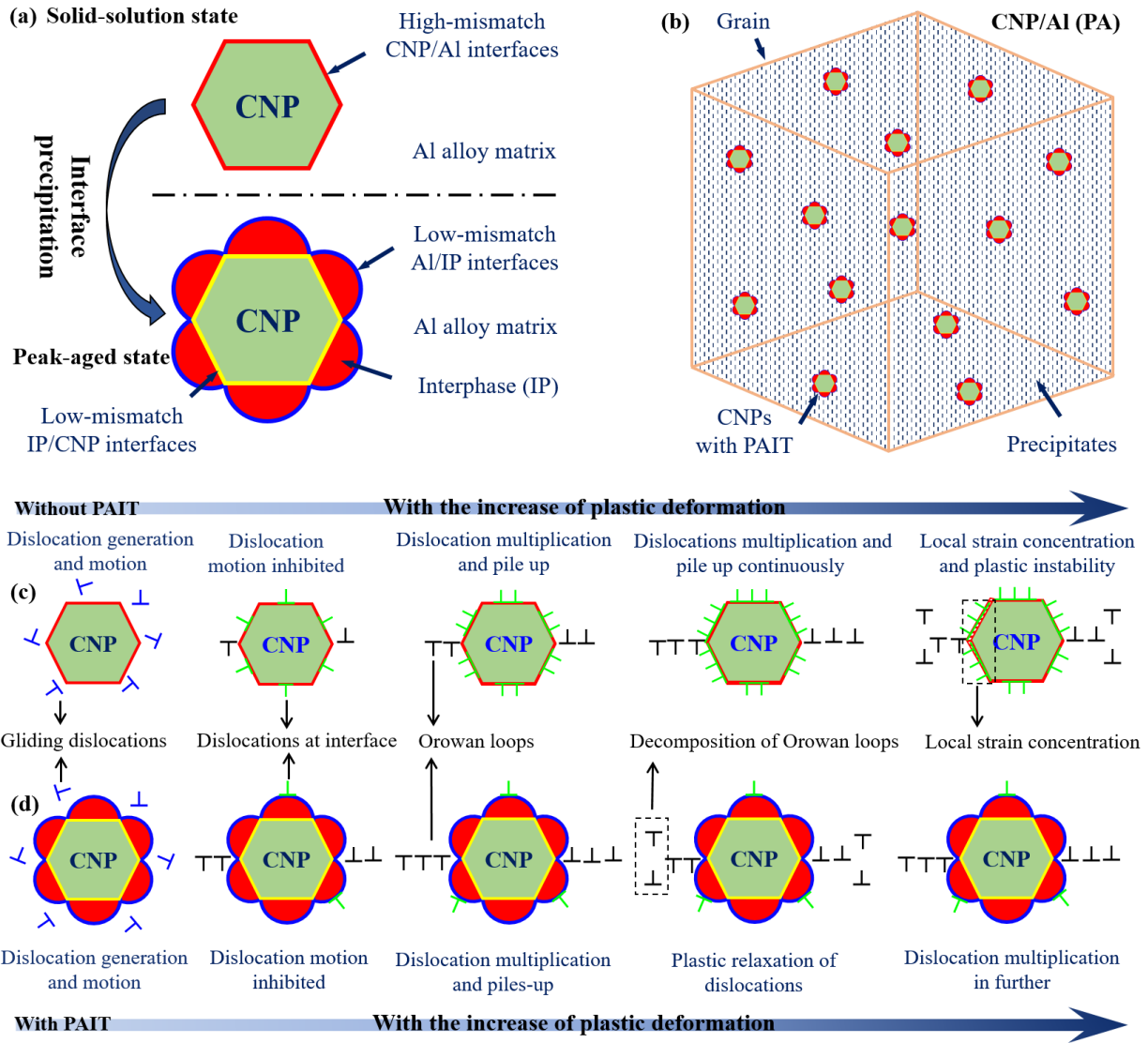


Fig. 12 Schematic illustrations of the proposed PAIT mechanism in the CNP/7075Al composite: (a) high mismatch CNP/Al interfaces are tailored by interface precipitation during the peak aging treatment; (b) overview of both tailored CNPs along with homogeneous nanoprecipitates dispersed in the matrix during peak aging; (c) and (d) dislocation structure evolution of MMCs without PAIT and with PAIT mechanisms during plastic deformation, respectively.

However, with the increase of deformation, most of dislocations are accumulated surrounding the CNP/IP/Al multi-interfaces in terms of Orowan loops (Fig. 12(d)), which differs from the high mismatch CNP/Al interface. With further increasing the strain, the accumulated Orowan loops can relieve internal stress without strain localization at CNP/IP/Al interfaces since the Orowan loops can decompose into prismatic loops [80,81] (Fig. 12(d)). The decomposition



of Orowan loops also provides a new room for the dislocation multiplication and annihilation, delaying the occurrence of plastic instability and achieving higher ductility (Fig. 12(d)).

To validate the above discussions, we measured the dislocation densities of the TiB<sub>2</sub>/7075Al-WQ and TiB<sub>2</sub>/7075Al-PA samples after the tensile tests using SRXRD (Fig. S2). Their initial dislocation densities are almost the same before tensile deformation. After tensile fracture (measured next to fracture surface), the dislocation density of the TiB<sub>2</sub>/7075Al-WQ ( $9.4 \times 10^{14} \text{ m}^{-2}$ ) is much higher than that of the TiB<sub>2</sub>/7075Al-PA ( $5.1 \times 10^{14} \text{ m}^{-2}$ ). This verifies the higher dynamic recovery rate of the TiB<sub>2</sub>/7075Al-PA sample, limiting the rapid increase in dislocation density during tensile deformation. The activation of plastic relaxation mechanism provides the new room for dislocation proliferation. Thus, the TiB<sub>2</sub>/7075-PA composite sustains a relatively higher work hardening rate during deformation and possesses a good ductility.

In summary, the highly coherent IP is introduced to improve the interface coherency and strength, so as to change the behaviors of dislocation motion and proliferation. As a result, the TiB<sub>2</sub>/7075Al-PA composite with CNPs/IP/Al multi-interfaces has a higher dynamic recovery rate of dislocation, and could provide new room for continuous dislocation proliferation and annihilation, and thus leading to a higher work hardening rate. The mechanism for the strategy used for enhancing strength and ductility is defined as precipitation-assisted interface tailoring (PAIT) mechanism.

## 5. Conclusions

In this study, we proposed an effective strategy to break down the long-standing strength-ductility trade-off in conventional MMCs by tailoring the CNP/matrix interface. We clarified the PAIT mechanism of which the CNP/matrix interface with higher coherency can be designed by the E2EM model and achieved by IP precipitation. Notably, only the acquisition of fine (a few micron) equiaxed grains in the matrix is considered, which rules out the similarities compared with any strategies ever reported in nanocrystalline materials and opens a new avenue to break down the strength-ductility trade-off in engineering materials. The main conclusions are summarized as follows:

(1) The TiB<sub>2</sub>/IP/Al multi-interfaces form due to the introduction of IP in the designed TiB<sub>2</sub>/7075Al composite by using conventional and upscalable processing processes including casting, FSP, hot extrusion with PA. This IP is identified as Mg(Zn<sub>1.5</sub>Cu<sub>0.5</sub>) phase.

(2) The interface coherency and interface strength of  $\text{TiB}_2/\text{IP}/\text{Al}$  multi-interfaces are enhanced evidently compared with traditional  $\text{TiB}_2/\text{Al}$  interface in MMCs. The original  $\text{TiB}_2/\text{Al}$  interface parallel to the prismatic  $\{01\bar{1}0\}_{\text{TiB}_2}$  facet shows a high mismatch of 38.03 %, while the newly formed  $\text{TiB}_2/\text{IP}$  interface  $(01\bar{1}0)_{\text{TiB}_2} // (11\bar{2}8)_{\text{IP}}$  and  $\text{IP}/\text{Al}$  interface  $(11\bar{2}4)_{\text{IP}} // (11\bar{1})_{\text{Al}}$  show much lower mismatch values of 2.94 % and 0.08 %, respectively.

(3) The designed  $\text{TiB}_2/7075\text{Al-PA}$  exhibits a higher combination of strength and ductility (yield stress~ 610 MPa; uniform elongation~11.5%) due to the PAIT mechanism, which stand out from most available Al-based materials. Due to the introduction of IP, the interface strength of  $\text{TiB}_2/\text{IP}/\text{Al}$  multi-interfaces increases, which leads to about fivefold load-bearing strengthening increment compared with the conventional composite with only the  $\text{TiB}_2/\text{Al}$  interface.

(4) The highly coherent  $\text{TiB}_2/\text{IP}/\text{Al}$  interfaces change the behaviors of dislocation motion and proliferation. More dislocations are stored within such interfaces in terms of Orowan loops during deformation, rather than being piled up within the  $\text{TiB}_2/\text{Al}$  interface. As a consequence, the designed composite exhibits the higher work hardening rate through effectively promoting dislocation multiplication and annihilation, thus leading to a higher ductility.

## References

- [1] R.O. Ritchie, The conflicts between strength and toughness, *Nat. Mater.* 10 (2011) 817-822.
- [2] E. Ma, T. Zhu, Towards strength–ductility synergy through the design of heterogeneous nanostructures in metals, *Mater. Today* 20 (2017) 323-331.
- [3] I.A. Ovid'ko, R.Z. Valiev, Y.T. Zhu, Review on superior strength and enhanced ductility of metallic nanomaterials, *Prog. Mater. Sci.* 94 (2018) 462-540.
- [4] L.G. Sun, G. Wu, Q. Wang, J. Lu, Nanostructural metallic materials: Structures and mechanical properties, *Mater. Today* 38 (2020) 114-135.
- [5] Z. Cheng, H. Zhou, Q. Lu, H. Gao, L. Lu, Extra strengthening and work hardening in gradient nanotwinned metals, *Science* 362 (2018) eaau1925.
- [6] K. Lu, Making strong nanomaterials ductile with gradients, *Science* 345 (2014) 1455-1456.
- [7] X. Wu, M. Yang, F. Yuan, G. Wu, Y. Wei, X. Huang, Y. Zhu, Heterogeneous lamella structure unites ultrafine-grain strength with coarse-grain ductility, *Proc. Natl. Acad. Sci.* 112 (2015) 14501-14505.
- [8] Y.M. Wang, T. Voisin, J.T. McKeown, J. Ye, N.P. Calta, Z. Li, Z. Zeng, Y. Zhang, W. Chen, T.T. Roehling, R.T. Ott, M.K. Santala, P.J. Depond, M.J. Matthews, A.V. Hamza, T. Zhu, Additively manufactured hierarchical stainless steels with high strength and ductility, *Nat. Mater.* 17 (2018) 63-71.
- [9] R. Ding, Y. Yao, B. Sun, G. Liu, J. He, T. Li, X. Wan, Z. Dai, D. Ponge, D. Raabe, Chemical boundary engineering: A new route toward lean, ultrastrong yet ductile steels, *Sci. Adv.* 6 (2020) eaay1430.

- [10] L.Y. Chen, J.Q. Xu, H. Choi, M. Pozuelo, X. Ma, S. Bhowmick, J.M. Yang, S. Mathaudhu, X.C. Li, Processing and properties of magnesium containing a dense uniform dispersion of nanoparticles, *Nature* 528 (2015) 539-543.
- [11] X.L. Zhong, W.L.E. Wong, M. Gupta, Enhancing strength and ductility of magnesium by integrating it with aluminum nanoparticles, *Acta Mater.* 55 (2007) 6338-6344.
- [12] R. Xu, G. Fan, Z. Tan, G. Ji, C. Chen, B. Beausir, D.B. Xiong, Q. Guo, C. Guo, Z. Li, D. Zhang, Back stress in strain hardening of carbon nanotube/aluminum composites, *Mater. Res. Lett.* 6 (2017) 113-120.
- [13] J. Liu, Z. Chen, F. Zhang, G. Ji, M. Wang, Y. Ma, V. Ji, S. Zhong, Y. Wu, H. Wang, Simultaneously increasing strength and ductility of nanoparticles reinforced Al composites via accumulative orthogonal extrusion process, *Mater. Res. Lett.* 6 (2018) 406-412.
- [14] S.C. Tjong, Novel nanoparticle-reinforced metal matrix composites with enhanced mechanical properties, *Adv. Eng. Mater.* 9 (2007) 639-652.
- [15] C. He, N. Zhao, C. Shi, X. Du, J. Li, H. Li, Q. Cui, An approach to obtaining homogeneously dispersed carbon nanotubes in Al powders for preparing reinforced Al-matrix composites, *Adv. Mater.* 19 (2007) 1128-1132.
- [16] Y. Min, M. Akbulut, K. Kristiansen, Y. Golan, J. Israelachvili, The role of interparticle and external forces in nanoparticle assembly, *Nat. Mater.* 7 (2008) 527-538.
- [17] J.Q. Xu, L.Y. Chen, H. Choi, X.C. Li, Theoretical study and pathways for nanoparticle capture during solidification of metal melt, *J. Phys: Condens. Mat.* 24 (2012) 255304.
- [18] L. Jiang, H. Wen, H. Yang, T. Hu, T. Topping, D. Zhang, E.J. Lavernia, J.M. Schoenung, Influence of length-scales on spatial distribution and interfacial characteristics of B<sub>4</sub>C in a nanostructured Al matrix, *Acta Mater.* 89 (2015) 327-343.
- [19] S. Lartigue-Korinek, M. Walls, N. Haneche, L. Cha, L. Mazerolles, F. Bonnet, Interfaces and defects in a successfully hot-rolled steel-based composite Fe-TiB<sub>2</sub>, *Acta Mater.* 98 (2015) 297-305.
- [20] I.J. Beyerlein, M.J. Demkowicz, A. Misra, B. Uberuaga, Defect-interface interactions, *Prog. Mater. Sci.* 74 (2015) 125-210.
- [21] M. Ashby, Work hardening of dispersion-hardened crystals, *Philos. Mag.* 14 (1966) 1157-1178.
- [22] L. Brown, Precipitation and dispersion hardening, *Strength of metals and alloys*, Pergamon Press, 1979.
- [23] L. Jiang, H. Yang, J.K. Yee, X. Mo, T. Topping, E.J. Lavernia, J.M. Schoenung, Toughening of aluminum matrix nanocomposites via spatial arrays of boron carbide spherical nanoparticles, *Acta Mater.* 103 (2016) 128-140.
- [24] S.C. Tjong, Z. Ma, Microstructural and mechanical characteristics of in situ metal matrix composites, *Mater. Sci. Eng. R* 29 (2000) 49-113.
- [25] B.S. Murty, S.A. Kori, M. Chakraborty, Grain refinement of aluminium and its alloys by heterogeneous nucleation and alloying, *Int. Mater. Rev.* 47 (2002) 3-29.
- [26] S. Ma, P. Zhang, G. Ji, Z. Chen, G. Sun, S. Zhong, V. Ji, H. Wang, Microstructure and mechanical properties of friction stir processed Al-Mg-Si alloys dispersion-strengthened by nanosized TiB<sub>2</sub> particles, *J. Alloy. Compd.* 616 (2014) 128-136.
- [27] M.B. Lezaack, F. Hannard, L. Zhao, A. Orekhov, J. Adrien, A. Miettinen, H. Idrissi, A. Simar, Towards ductilization of high strength 7XXX aluminium alloys via microstructural modifications obtained by friction stir processing and heat treatments, *Materialia* 20 (2021) 101248.
- [28] P.L. Schaffer, D.N. Miller, A.K. Dahle, Crystallography of engulfed and pushed TiB<sub>2</sub> particles in aluminium, *Scr. Mater.* 57 (2007) 1129-1132.

- [29] G. Ribárik, T. Ungár, J. Gubicza, G.R. Rik, T. Unga, MWP-fit: a program for multiple whole-profile fitting of diffraction peak profiles by ab initio theoretical functions, *J. Appl. Crystallogr.* 34 (2010) 669-676.
- [30] T. Ungár, J. Gubicza, G. Ribárik, A. Borbély, Crystallite size distribution and dislocation and dislocation structure determined by diffraction profile analysis-principles and practical application to cubic and hexagonal crystals, *J. Appl. Crystallogr.* 34 (2001) 298-310.
- [31] G. Ribárik, Modeling of diffraction patterns based on microstructural properties, Eötvös Loránd University, Thesis of PhD, 2008, pp.42-57.
- [32] Y. Ji, M.X. Zhang, H. Ren, Roles of lanthanum and cerium in grain refinement of steels during solidification, *Metals* 8 (2018) 884.
- [33] Y. Ma, A. Addad, G. Ji, M.X. Zhang, W. Lefebvre, Z. Chen, V. Ji, Atomic-scale investigation of the interface precipitation in a TiB<sub>2</sub> nanoparticles reinforced Al–Zn–Mg–Cu matrix composite, *Acta Mater.* 185 (2020) 287-299.
- [34] M.X. Zhang, P. Kelly, M. Easton, J. Taylor, Crystallographic study of grain refinement in aluminum alloys using the edge-to-edge matching model, *Acta Mater.* 53 (2005) 1427-1438.
- [35] G.G. Kresse, J.J. Furthmüller, Efficient iterative schemes for Ab initio total-energy calculations using a plane-wave basis set, *Phys. Rev. B* 54 (1996) 11169.
- [36] G.J. Kresse, D.P. Joubert, From ultrasoft pseudopotentials to the projector augmented-wave method, *Phys. Rev. B* 59 (1999) 1758-1775.
- [37] J.P. Perdew, K. Burke, M. Ernzerhof, Generalized gradient approximation made simple, *Phys. Rev. Lett.* 77 (1996) 3865-3868.
- [38] Y. Tang, Z. Chen, A. Borbély, G. Ji, S.Y. Zhong, D. Schryvers, V. Ji, H.W. Wang, Quantitative study of particle size distribution in an in-situ grown Al–TiB<sub>2</sub> composite by synchrotron X-ray diffraction and electron microscopy, *Mater. Charact.* 102 (2015) 131-136.
- [39] M. Ellner, B. Predel, Neutron-diffraction analysis of ternary laves phases of the MgCu<sub>2</sub> type, *J. Solid State Chem.* 30 (1979) 209-221.
- [40] G. Liu, J. Geng, Y. Li, L. Cai, M. Wang, D. Chen, N. Ma, H. Wang, Effects of pre-strain on the microstructural evolution and mechanical strength of in situ TiB<sub>2</sub>/7050 Al composite, *Adv. Eng. Mater.* 21 (2019) 1900042.
- [41] D.A. Porter, K.E. Easterling, Phase transformations in metals and alloys, Chapman & Hall Press, 1992.
- [42] JCPDS-International centre for diffraction data, PCPDFWIN, Version 2.3, 2002.
- [43] J.W. Christian, The theory of transformations in metals and alloys, Pergamon, 2002.
- [44] W. Sun, Y. Zhu, R. Marceau, L. Wang, Q. Zhang, X. Gao, C. Hutchinson, Precipitation strengthening of aluminum alloys by room-temperature cyclic plasticity, *Science* 363 (2019) 972-975.
- [45] Y. Zhao, X. Liao, Z. Jin, R. Valiev, Y.T. Zhu, Microstructures and mechanical properties of ultrafine grained 7075 Al alloy processed by ECAP and their evolutions during annealing, *Acta Mater.* 52 (2004) 4589-4599.
- [46] Y.H. Zhao, X.Z. Liao, S. Cheng, E. Ma, Y.T. Zhu, Simultaneously increasing the ductility and strength of nanostructured alloys, *Adv. Mater.* 18 (2006) 2280-2283.
- [47] Z.Y. Liu, K. Ma, G.H. Fan, K. Zhao, J.F. Zhang, B.L. Xiao, Z.Y. Ma, Enhancement of the strength-ductility relationship for carbon nanotube/Al–Cu–Mg nanocomposites by material parameter optimisation, *Carbon* 157 (2020) 602-613.

- [48] B. Han, E. Lavernia, Z. Lee, S. Nutt, D. Witkin, Deformation behavior of bimodal nanostructured 5083 Al alloys, *Metall. Mater. Trans. A* 36 (2005) 957-965.
- [49] K. Kempen, L. Thijs, J. Van Humbeeck, J.P. Kruth, Mechanical properties of AlSi10Mg produced by selective laser melting, *Physics Procedia* 39 (2012) 439-446.
- [50] J.H. Martin, B.D. Yahata, J.M. Hundley, J.A. Mayer, T.A. Schaedler, T.M. Pollock, 3d printing of high-strength aluminium alloys, *Nature* 549 (2017) 365-369.
- [51] D.L. McDanel, Analysis of stress-strain, fracture, and ductility behavior of aluminum matrix composites containing discontinuous silicon carbide reinforcement, *Metall. Trans. A* 16 (1985) 1105-1115.
- [52] J.K. Shang, R. Ritchie, On the particle-size dependence of fatigue-crack propagation thresholds in SiC-particulate-reinforced aluminum-alloy composites: role of crack closure and crack trapping, *Acta Metall.* 37 (1989) 2267-2278.
- [53] Y. Ma, Z. Chen, M. Wang, D. Chen, N. Ma, H. Wang, High cycle fatigue behavior of the in-situ TiB<sub>2</sub>/7050 composite, *Mater. Sci. Eng. A* 640 (2015) 350-356.
- [54] Q. Yang, Y. Shen, J. Liu, L. Wang, Z. Chen, M.L. Wang, S.Y. Zhong, Y. Wu, H.W. Wang, Microstructure and mechanical response of TiB<sub>2</sub>/Al-Zn-Mg-Cu composites with more addition of Zn, *J. Alloy. Compd.* 816 (2020) 152584.
- [55] H. Wei, Z. Li, D.B. Xiong, Z. Tan, G. Fan, Z. Qin, D. Zhang, Towards strong and stiff carbon nanotube-reinforced high-strength aluminum alloy composites through a microlaminated architecture design, *Scr. Mater.* 75 (2014) 30-33.
- [56] B. Chen, J. Shen, X. Ye, L. Jia, S. Li, J. Umeda, M. Takahashi, K. Kondoh, Length effect of carbon nanotubes on the strengthening mechanisms in metal matrix composites, *Acta Mater.* 140 (2017) 317-325.
- [57] U.F. Kocks, Laws for work-hardening and low-temperature creep, *J. Eng. Mater. Technol.* 98 (1976) 76-85.
- [58] G.I. Taylor, The mechanism of plastic deformation of crystals. Part I. Theoretical, *Proc. R. Soc. A* 145 (1934) 362-387.
- [59] K. Ma, H. Wen, T. Hu, T.D. Topping, D. Isheim, D.N. Seidman, E.J. Lavernia, J.M. Schoenung, Mechanical behavior and strengthening mechanisms in ultrafine grain precipitation-strengthened aluminum alloy, *Acta Mater.* 62 (2014) 141-155.
- [60] E. Voce, The relationship between stress and strain for homogeneous deformation, *J. Inst. Met.* 74 (1948) 537-562.
- [61] G. Sha, A. Cerezo, Early-stage precipitation in Al-Zn-Mg-Cu alloy (7050), *Acta Mater.* 52 (2004) 4503-4516.
- [62] G. Sha, A. Cerezo, Kinetic Monte Carlo simulation of clustering in an Al-Zn-Mg-Cu alloy (7050), *Acta Mater.* 53 (2005) 907-917.
- [63] C. Wolverton, Crystal structure and stability of complex precipitate phases in Al-Cu-Mg-(Si) and Al-Zn-Mg alloys, *Acta Mater.* 49 (2001) 3129-3142.
- [64] E.O. Hall, The deformation and ageing of mild steel: III discussion of results, *Proc. R. Soc. B* 64 (1951) 747-753.
- [65] N.J. Petch, The cleavage strength of polycrystals. *J. Iron Steel Inst.* 174 (1953) 25-28.
- [66] R.L. Fleischer, Substitutional solution hardening, *Acta Metall.* 11 (1963) 203-209.
- [67] K. Ma, T. Hu, H. Yang, T. Topping, A. Yousefiani, E.J. Lavernia, J.M. Schoenung, Coupling of dislocations and precipitates: Impact on the mechanical behavior of ultrafine grained Al-Zn-Mg alloys, *Acta Mater.* 103 (2016) 153-164.

- [68] H. Wen, T.D. Topping, D. Isheim, D.N. Seidman, E.J. Lavernia, Strengthening mechanisms in a high-strength bulk nanostructured Cu–Zn–Al alloy processed via cryomilling and spark plasma sintering, *Acta Mater.* 61 (2013) 2769-2782.
- [69] A.J. Ardell, Precipitation hardening, *Metall. Trans. A* 16A (1985) 2131-2165.
- [70] H. Chen, Z. Chen, G. Ji, S. Zhong, H. Wang, A. Borbély, Y. Ke, Y. Bréchet, Experimental and modelling assessment of ductility in a precipitation hardening AlMgScZr alloy, *Int. J. Plasticity* 139 (2021) 102971.
- [71] H. Chen, Z. Chen, G. Ji, S. Zhong, H. Wang, A. Borbély, Y. Ke, Y. Bréchet, The influence of shearable and nonshearable precipitates on the Portevin-Le Chatelier behavior in precipitation hardening AlMgScZr alloys, *Int. J. Plasticity* 147 (2021) 103120.
- [72] R. Alizadeh, J. Llorca, Interactions between basal dislocations and  $\beta 1'$  precipitates in Mg–4Zn alloy: Mechanisms and strengthening, *Acta Mater.* 186 (2020) 475-486.
- [73] N. Li, C. Wang, M.A. Monclús, L. Yang, J.M. Molina-Aldareguia, Solid solution and precipitation strengthening effects in basal slip, extension twinning and pyramidal slip in Mg–Zn alloys, *Acta Mater.* 221 (2021) 117374.
- [74] X.P. Li, G. Ji, Z. Chen, A. Addad, Y. Wu, H.W. Wang, J. Vleugels, J. Van Humbeeck, J.P. Kruth, Selective laser melting of nano-TiB<sub>2</sub> decorated AlSi10Mg alloy with high fracture strength and ductility, *Acta Mater.* 129 (2017) 183-193.
- [75] A. Ghosh, M. Ghosh, G. Shankar, On the role of precipitates in controlling microstructure and mechanical properties of Ag and Sn added 7075 alloys during artificial ageing, *Mater. Sci. Eng. A* 738 (2018) 399-411.
- [76] T. Yang, Y.L. Zhao, Y. Tong, Z.B. Jiao, J. Wei, J.X. Cai, X.D. Han, D. Chen, A. Hu, J.J. Kai, K. Lu, Y. Liu, C.T. Liu, Multicomponent intermetallic nanoparticles and superb mechanical behaviors of complex alloys, *Science* 362 (2018) 933-937.
- [77] J. Wang, Q. Zhou, S. Shao, A. Misra, Strength and plasticity of nanolaminated materials, *Mater. Res. Lett.* 5 (2016) 1-19.
- [78] L.M. Brown, G.R. Woolhouse, The loss of coherency of precipitates and the generation of dislocations, *Philos. Mag.* 21 (2006) 329-345.
- [79] R.G. Hoagland, T.E. Mitchell, J.P. Hirth, H. Kung, On the strengthening effects of interfaces in multilayer fee metallic composites, *Philos. Mag.* 82 (2002) 643-664.
- [80] L.M. Brown, W.M. Stobbs, The work-hardening of copper-silica, *Philos. Mag.* 23 (1971) 1201-1233.
- [81] P.B. Hirsch, F.J. Humphreys, The deformation of single crystals of copper and copper-zinc alloys containing alumina particles II. Microstructure and dislocation-particle interactions, *Proc. R. Soc. A* 318 (1970) 73-92.

## Acknowledgements

Y. Ma is grateful for his Ph.D. project supported by the China Scholarship Council (Grant no. 201606230212). This work is partially supported by the National Natural Science Foundation of China [Grant No. 51971137]. We would like to thank the beamtime at HEMS P07B at DESY and the instrument responsible Dr. E. Maawad for his kind support during the synchrotron test. Many thanks are due to Prof. C. Hutchinson for providing us original data of tensile tests. The Chevreul Institute is thanked for its help in the development of this work through the ARCHI-

CM project supported by the “Ministère de l’Enseignement Supérieur de la Recherche et de l’Innovation”, the region “Hauts-de-France”, the ERDF program of the European Union and the “Métropole Européenne de Lille”.